

# Supermodeling of tumor dynamics with parallel isogeometric analysis solver

Leszek Siwik<sup>a</sup>, Marcin Łoś<sup>a</sup>, Adrian Kłusek<sup>a</sup>,  
Witold Dzwinel<sup>a</sup>, Maciej Paszyński<sup>a</sup>, Keshav Pingali<sup>b</sup>

<sup>a</sup>*AGH University of Sciences and Technology  
Faculty of Computer Science, Electronics and Telecommunication  
Department of Computer Science  
al. A Mickiewicza 30, 30-059 Krakow, Poland  
email: maciej.paszynski@agh.edu.pl, phone: +48-12-328-3314, fax: +48-12-617-5172*  
<sup>b</sup>*The University of Texas at Austin  
Institute for Computational and Engineering Sciences*

---

## Abstract

In this paper, for the first time, we propose the supermodeling algorithm which couples and synchronizes three-dimensional isogeometric analysis simulators. We focus on the computational oncology and we show that it is possible to obtain reliable prognoses about cancer dynamics by creating the supermodel of cancer. It consists of several coupled instances (the sub-models) of a generic cancer model, developed with the isogeometric analysis. The supermodel integrates with real data by employing a prediction/correction learning scheme focused on fitting several values of coupling coefficients between sub-models. This supermodel data assimilation is an alternative to the classical methods matching scores (even hundreds) of tumor model parameters. We show that the isogeometric analysis is a proper tool to develop a generic computer model of cancer, which can be a computational framework for developing high-quality supermodels. We believe that the latent fine-grained tumor features, e.g., microscopic processes and other unpredictable events accompanying its proliferation not included in the model (that is, not involved directly in the mathematical model), are present in incoming real data and will still influence in indirect way tumor dynamics.

**Keywords:** isogeometric analysis, tumor growth simulation, supermodeling, data assimilation, GPGPU, GLUON environment

---

## 1. Introduction

Data assimilation is the key component of computer tumor simulations [1]. The modern computer simulators of tumor dynamics such as but not limited to [2, 3, 4, 5, 6, 7, 8, 9, 10, 11, 12, 22] have several dozens of parameters that have to be adjusted to match with medical measurements, e.g., resulting from the MRI scans of the tumor obtained within some time intervals from patients.

For this inverse problem, we define the fitness function as some measure between the numerical simulations and measurement data. We are looking for such a set of parameters of the mathematical model, which minimizes this discrepancy. We seek for proper values of the model parameters. This is obvious that such a problem is ill-conditioned, and the solutions' space "explodes" with an increasing number of model parameters. Classical data assimilation algorithms result in prohibitively long computations [23, 24, 25, 26]. We can solve the inverse problem by using either simple [36] or hybrid hierarchical genetic algorithm [37]. Moreover, the inverse problem may encounter a vast number of local minima, where our algorithm may get stuck. In such a case, we obtain an imperfect approximation of the ground truth (GT). Thus, the single tumor model itself may not be able to match the reality with adequate precision. Even if we find an excellent solution to our inverse problem, it may still be far from the real data that we want to match. This paper's main contribution is to propose the supermodeling as a second abstraction layer to standard data assimilation procedures, which can improve their quality and computational performance.

This approach was first proposed to deal with climate simulations [13, 27, 28, 29, 30]. The idea of the application of the supermodeling for tumor simulations was described in [20, 21]. Herein, for the first time, we apply the supermodeling which couples and synchronizes three-dimensional isogeometric analysis simulators. Namely, we couple and synchronize tumor models realized numerically by using the isogeometric finite element method solver [12] implemented in GALOIS [18, 19].

Our mathematical model of tumor dynamics uses the set of parabolic PDEs (mainly reaction-diffusion type) representing concentration fields (densities) of: tumor cells, tumor angiogenic factor (TAF), oxygen concentration, extracellular matrix, and the degraded extracellular matrix. The model has over twenty model parameters. Our goal is to simulate the tumor progression, similar as much as possible to the realistic patterns. Before the process

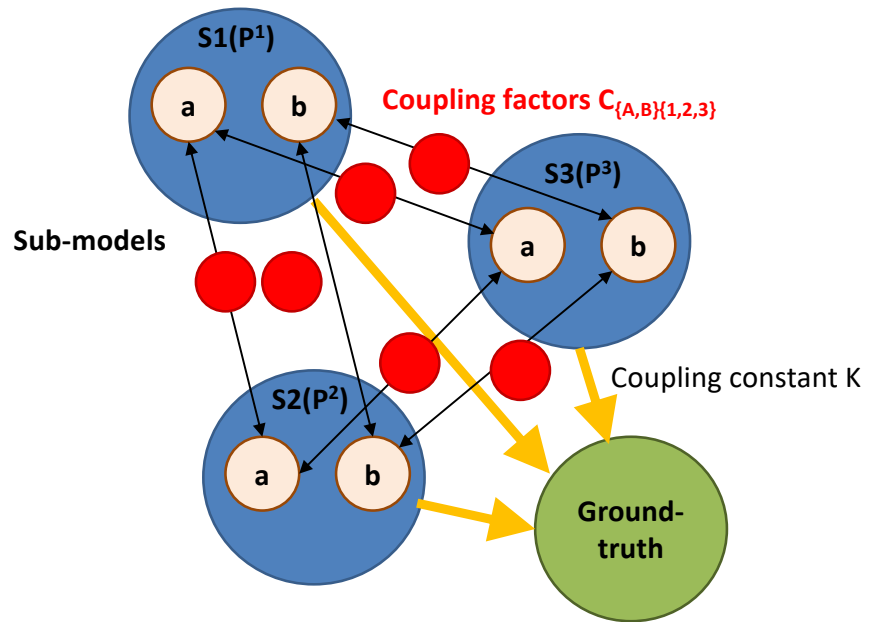


Figure 1: Coupling of three sub-models and the ground-truth.

of data assimilation, we propose to perform the sensitivity analysis of our tumor model first [31, 32]. Finding the most sensitive parameters and dynamic variables allows us to focus better on the data adaptation process and thus to save computational time. Knowing the most important dynamic variables enables us to construct the most parsimonious (in terms of the number of sub-models connections) supermodel. We identify the four most sensitive parameters. These are: tumor cell proliferation time, tumor cell survival time, threshold oxygen concentration for tumor cells to multiply, or die. On this basis, we set up three (sub)models being instances of the same model with different values of (most sensitive) parameters so resulting in different tumor growth evolution. Next, we construct the supermodel by coupling the dynamic variables as well as by coupling the sub-models with the ground truth data. As shown in Figure 1, three sub-models with parameters sets S1, S2, and S3 are connected. They create the supermodel through dynamic variables A and B. The strength of couplings is represented by the coupling matrix C. In case of coupling continuous models of tumor dynamics, like e.g., isogeometric analysis simulator using reaction-diffusion models, the dynamic variable is a scalar field, which for each time step is represented by a linear combination of B-spline basis functions over three-dimensional cube shape domain. We have a one-dimensional basis along  $x$ ,  $y$ , and  $z$  directions

$$\{B_{i,p}^x\}_{i=1,\dots,N_e+p}, \{B_{i,p}^y\}_{i=1,\dots,N_e+p}, \{B_{i,p}^z\}_{i=1,\dots,N_e+p} \quad (1)$$

resulting in a tensor product three-dimensional B-spline basis of order  $p$  with respect to each variable

$$\{B_{i,p}^x B_{j,p}^y B_{k,p}^z\}_{i,j,k=1,\dots,N_e+p} \quad (2)$$

In particular, for mesh size of  $N_e^3$  where  $N_e$  is the number of elements in one direction, we have  $(N_e + p)^3$  coefficients, for each time step, e.g., for the tumor density field

$$b(x, y, z; t) = \sum_{i,j,k=1,\dots,N_e+p} b_{i,j,k}(t) B_{i,p}^x B_{j,p}^y B_{k,p}^z. \quad (3)$$

Thus, for the mesh dimension  $N_e = 120$  and quadratic B-splines, the supermodel in this continuous setup requires a coupling of  $(120 + 2)^3 = 122^3 = 1,815,848$  double-precision unknowns. In the case considered in this paper, we couple a couple of tumor density scalar fields, which means that we

couple millions of double precision variables, representing the coefficients of B-spline spans over 3D mesh every time step. We train the matrix to obtain the best synchronization between the sub-models. The training nudges the supermodel of synchronized sub-models towards the ground truth data. The value of nudging factor  $K$  is the learning rate, selected as a constant during training. Since the (sub)models are coupled only by the most sensitive variables; it eliminates the number of coupling factors.

We employed the learning scheme to fit both, the sub-models coupling parameters and training constants, to the ground truth data. We employ the ground truth the tumor dynamics snapshots (the number of tumor cells) simulated by our tumor model with the reference parameter set.

Thus, by using the supermodeling approach, we can simulate this reality by synchronizing, in a nonlinear way, a few different models. In particular, we applied the high fidelity model running on a cluster of GPUs [22], so we have got the linear combinations of B-splines representing the tumor density field over the larger computational mesh  $b^{HF}(x, y, z; t) = \sum_{i,j,k=1,\dots,(N_e^{HF}+p)} b_{i,j,k}^{HF}(t) B_{i,p}^x(x) B_{j,p}^y(y) B_{k,p}^z(z)$ , where  $N_e^{HF}$  represents the number of elements in the high-fidelity results, and  $p$  represents the B-splines order. Later, we project this solution using the isogeometric  $L^2$  projection into the computational mesh used during the supermodeling, to get  $b^{GT}(x, y, z; t) = \sum_{i,j,k=1,\dots,(N_e+p)} b_{i,j,k}^{GT}(t) B_{i,p}^x(x) B_{j,p}^y(y) B_{k,p}^z(z)$ , where  $N_e$  represents the number of elements over the mesh using during the supermodeling simulations. In other words, we speed up data assimilation for a complex multi-parameter dynamical process by adding the supermodeling abstraction layer.

## 2. Key issues in supermodeling

The supermodel, illustrated in Figure 1, is composed of several (e.g. three) sub-models  $\mathbf{S1}(\mathbf{P}^1), \mathbf{S2}(\mathbf{P}^2), \mathbf{S3}(\mathbf{P}^3)$ . In general, these sub-models can represent various and heterogeneous models of tumor described by different sets of PDEs [8, 9, 10, 11] (provided that there exist similar dynamical variables which can be coupled), however, in case of data adaptation, they may also be defined as the same set of PDEs with different parameter values [12] what we are examining in this paper. Of course, various parametrization results in various tumor dynamics. Thus, we may have a few homogeneous sub-models with respective parameters sets  $P^1, P^2, P^3$ , with admissible values. These sub-models define the following dynamics variables: tumor cell

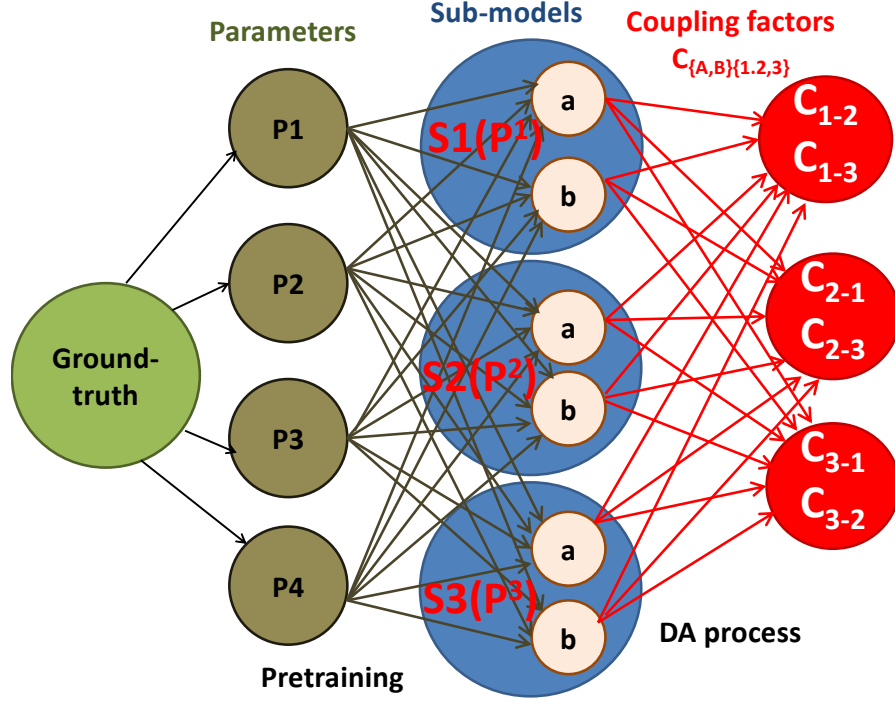


Figure 2: Creation of a supermodel.

density scalar field  $b$ , tumor angiogenic factor (TAF) concentration  $a$ , vasculature network, oxygen concentration, the density of extracellular, and degraded extracellular matrix. These dynamic variables are coupled by using the coupling constants  $C_{i,j}^a, C_{i,j}^b$ , where  $a$  and  $b$  denotes the coupled dynamic variables, and  $i, j$  denotes the pair of coupled sub-models. Finally, we couple all sub-models with the ground truth data, using the training constant (nudging coefficient)  $K$  that can be matched arbitrarily.

The general scheme demonstrating the construction of the supermodel is summarized in Figure 2. We start with the creation of some sub-models that try to match the ground truth, in our case, the numerical models of the tumor progression. These models may use the same or different sets of PDEs, e.g. kind of advection-diffusion-reaction models, as described in [8, 12], or Cahn-Hilliard type models, as described in [10, 11, 9]. Specific sets of parameters instantiate the models. There are, at least, a few methods to set up the "proper" sub-models.

1. We can select the parameters on the basis of general knowledge about the simulated process.
2. We can start with the "most probable" set of parameters reported in the previous research, and generate sub-models perturbing the most sensitive ones.
3. We can apply a standard data assimilation procedure, and pre-train the model within a short time. We can select as the sub-models the parameter sets attaining the best local minima of a loss function.

In case of applying these strategies, it is good to know the results of sensitivity analysis to optimize the search. We call this phase the pretraining. Having the three sub-models **S1**, **S2**, and **S3** with three sets of their parameters  $\mathbf{P}^1, \mathbf{P}^2, \mathbf{P}^3$  where:

$\mathbf{P}^M = (p_1^M, \dots, p_n^M)$ , we can execute the learning phase, where we intend to find the values of the coupling factors:

$C_{1-2}^a, C_{2-1}^a, C_{1-3}^a, C_{3-1}^a, C_{2-3}^a, C_{3-2}^a$ , and  $C_{1-2}^b, C_{2-1}^b, C_{1-3}^b, C_{3-1}^b, C_{2-3}^b, C_{3-2}^b$ .

In other words, we parameterize the models with sets of parameters, and we couple the models' output, expressed by selected dynamic variables. We run the three sub-models, and we find the values of the coupling parameters. Once we have the coupling factors learned, we can create the supermodel and use it for simulation.

These are the following questions to be addressed when we construct a supermodel:

- Which sub-models should we choose, heterogeneous or homogeneous?
- How many sub-models do we need, and how many teaching samples are necessary to find the coupling constants [21].
- How to select the sub-models, so their synchronized supermodel will fit the ground truth (the real data).
- How many dynamic variables should we couple? How do we perform the coupling? Should we make it strongly or weakly?
- What is the proper training procedure?

Different choices may lead to different supermodels, and there is no general answer to all these questions [33]. The general idea is to make predictions

more accurate. For example, the solution of the inverse problem may lead to several local minima. Each of these local minima may be far from the ground truth, but the supermodel can use these local minima as sub-models and may synchronize well with the reality. Herein, we utilize the isogeometric analysis solver with a 3D tumor model [12] parameterized with 21 model parameters. We use the supermodeling for prediction of the system trajectory. As ground truth, we use the results produced by multi-GPU tumor simulator [14] we had developed earlier.

We can select the sets of parameters for the sub-models in two ways. The first one is to choose a set of parameters for each sub-model randomly. The second way is to use pre-trained models as sub-models, using standard data assimilation procedures, e.g., resulting from inverse modeling and sensitivity analysis. In research reported in this paper, we used the second method from those enumerated earlier to set up the parameters of sub-models. The rule of thumb is that we want the sub-models to be close to different "good" local minima surrounding the ground truth, see Figure 3.

In the supermodel we couple the sub-models through only one but very sensitive variable, namely, the tumor density, to prevent the model from being over wired and computationally demanding.

### 3. Supermodel of tumor

We used the one-phase mathematical model of tumor dynamics, which is based on the previously published seminal papers [12, 12, 32].

Domain of the simulation is the cube  $\Omega = [0, 5000] \times [0, 5000] \times [0, 5000]$   $[\mu m] = 5mm \times 5mm \times 5mm$ .

In the model we consider the following main quantities:

- tumor cell density  $b$ ,
- tumor angiogenic factor (TAF)  $c$ ,
- endothelial cells network,
- oxygen  $o$ ,
- density of the extracellular matrix (ECM)  $M$ ,
- density of the degraded extracellular matrix (ECM)  $A$ .



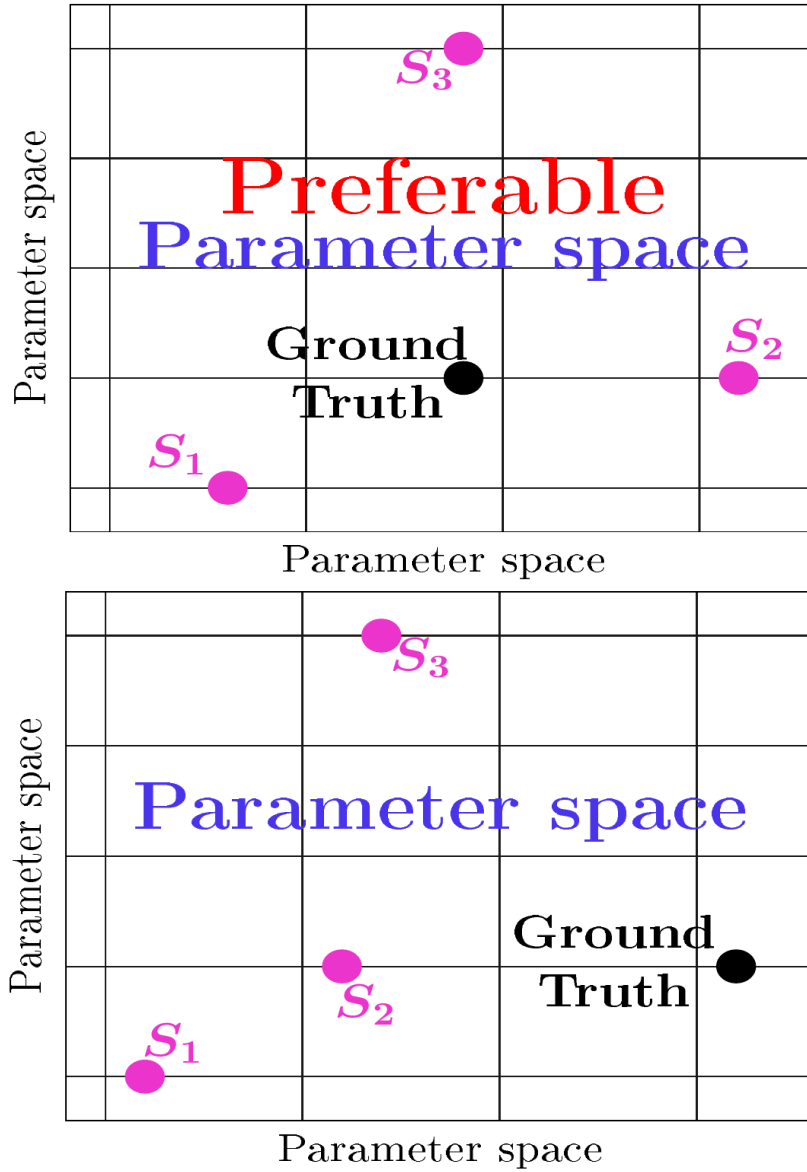


Figure 3: Selection of the sub-models with respect to the ground truth (GT). Preferable choice corresponds to the case when the GT is surrounded by sub-models, and thus it can be approximated by linear combination of sub-models.

There are also some auxiliary quantities, derived from the main quantities introduced above, i.e.:

- tumor cell sinks  $b^-$ ,
- tumor cell sources  $b^+$ ,
- tumor cell pressure  $P$ ,
- tumor cell flux  $J$ .

The regions where nutrients and oxygen are limited, the tumor cells produce TAFs which promote the proliferation of endothelial cells resulting in the formation of vessels.

The TAF concentration influences the growth of the vascular network by the discrete vascular model. It is governed by:

$$\frac{\partial c}{\partial t} = \chi_c \Delta c - \gamma_c o c + c^+ \quad (4)$$

where  $\chi_c$  denotes TAF diffusion rate,  $\gamma_c$  stands for TAF decay rate,  $c^+$  is the TAF “source”, where  $c^+ = b(1 - c)$  for  $o < o^{death}$ , and  $o^{death}$  is the TAF hypoxia rate.

The healthy cells, as well as tumor cells, live in the extracellular matrix  $M$ . The density of the extracellular matrix decreases when the tumor cells grow:

$$\frac{\partial M}{\partial t} = -\beta_M M b \quad (5)$$

where  $\beta_M$  denotes the ECM decay rate. On the other hand, the density of the degraded extracellular matrix increases with the density of the tumor cells, and it is expressed by the following formula:

$$\frac{\partial A}{\partial t} = \gamma_A M b + \chi_{aA} \Delta A - \gamma_{oA} A \quad (6)$$

where  $\gamma_A$  denotes the production rate of attractants,  $\chi_{aA}$  stands for diffusion rate of degraded extra-cellular matrix, and  $\gamma_{oA}$  is the decay rate of degraded extra-cellular matrix.

When the tumor cells grow over the normal tumor cell density, they impose the tumor cell pressure  $P$ . The tumor cell pressure varies linearly between 0 for the normal tumor cell density  $b^N = 1$ , up to 1, for the maximum

tumor cell density  $b^M = 2$ :

$$P = \begin{cases} 0 & \text{for } b < b^N \\ \frac{b-b^N}{b^M-b^N} & \text{for } b^N \leq b \leq b^M \end{cases} \quad (7)$$

The tumor cell pressure imposes the tumor cell flux  $J$ :

$$J = -D_b b (\nabla P + r_b \nabla A) \quad (8)$$

where  $D_b$  stands for the cell diffusion coefficient, which varies with the skin layer, and  $r_b$  denotes the tumor cell chemoattractant sensitivity.

Finally, the tumor cell density varies from  $b^m = 0$  representing the state with no cancer cells, to  $b^M = 2$  denoting the state with maximum tumor cell density. When the tumor cell density is larger than  $b^N = 1$ , it imposes the tumor cell pressure:

$$\frac{\partial b}{\partial t} = -\nabla \cdot J + b^- + b^+ \quad (9)$$

where  $J$  is the tumor cell flux, and  $b^+$ ,  $b^-$  describe tumor cell "sources" and "sinks", corresponding to cell proliferation (creation of new cells) and apoptosis (death of cells). The tumor pressure and interaction with degenerated extracellular matrix (ECM) induces the tumor flux, the oxygen supply governs sources and sinks. Tumor cell source and sink terms depend mostly on oxygen supply, and can be expressed by the following formulas:

$$\begin{aligned} b^+ &= \frac{b}{T^{prol}} \left( 1 + \frac{\tau_b A}{\tau_b A + 1} P_b \right) \left( 1 - \frac{b}{b^M} \right) & \text{for } o > o^{prol} \\ b^- &= -\frac{b}{T^{death}} & \text{for } o < o^{death} \end{aligned} \quad (10)$$

When oxygen level  $o$  exceeds  $o^{prol}$ , tumor cells proliferate. On the other hand, when  $o < o^{death}$ , tumor cells die. We compute the oxygen concentration  $o$  as:

$$\frac{\partial o}{\partial t} = \alpha_o \Delta o - \gamma_o b o + \delta_o (o^{\max} - o) o^{\text{src}} \quad (11)$$

where  $\alpha_o$  is the oxygen diffusion coefficient,  $\gamma_o$  is oxygen consumption rate,  $\delta_o$  describes how fast the oxygen is absorbed from the vasculature and  $o^{\max}$  is the maximal oxygen concentration. Value of  $o^{\text{src}}$  is 1 if there is a vessel in the specified point and 0 otherwise.

We introduce the vasculature as a discrete graph, with edges representing vessel segments and vertices corresponding to the vessel connections. This

graph is as a 3D bitmap of size  $K \times K \times K$ . Each cell is set to either 1 or 0, depending on the presence or absence of the vessel, respectively.

The main task of the vasculature is to provide oxygen to cells. The vasculature grows in response to the density of tumor cells and the presence of TAF. Vasculature evolution, similarly to the generation of the initial graph, has a stochastic nature and encompasses several processes:

- sprout creation,
- vessel degradation,
- vessel collapse,
- vessel dilatation.

All processes mentioned above, except the sprouting, are simulated at every simulation step. The vasculature grows in response to the presence of TAF. At each existing node a *sprout* may be created with probability  $\Delta t/t^{\text{sprout}}$ , provided the local TAF density exceeds  $c_{\min}$ . The direction of growth is given by  $\nabla c$ , which is a direction of the fastest growth of TAF and so points roughly to the nearby oxygen-starving cells. Length of the segment is given by  $l_{\text{seg}}$  and initial radius by  $r^{\text{sprout}}$ .

Vessels inside the region with a high density of tumor cells undergo a degradation. Each vessel segment has a stability coefficient  $w$ , initially  $w^{\text{init}}$ , that is decreased by  $w^{\text{deg}}\Delta t$  during each update if the local cancer cell density  $b$  exceeds  $b^{\text{norm}}$ .

When stability reaches 0, the vessel may collapse with probability  $\Delta t/t^{\text{coll}}$  – once that happens, we remove it from the vasculature graph.

If the vessel has been in a region with high tumor concentration ( $b > b^{\text{norm}}$ ) for at least  $t^{\text{switch}}$  hours, process of vessel dilatation is initiated. If value of TAF is sufficiently high ( $c > c^{\text{switch}}$ ), radius of the vessel is increased by  $\Delta r\Delta t$  each step, until it reaches maximum radius  $r^{\text{max}}$ .

For the detailed description of the model, we refer to [12].

Summing up, the model is described by the following set of mainly parabolic,

diffusion-reaction type of PDEs equations:

$$\left\{ \begin{array}{l} \frac{\partial b}{\partial t} = -\nabla \cdot J - \frac{b}{T^{death}} [o < o^{death}] + \\ \quad \frac{b}{T^{prol}} \left( 1 + \frac{\tau_b A}{\tau_b A + 1} P_b \right) \left( 1 - \frac{b}{b^M} \right) [o > o^{prol}] \\ \frac{\partial c}{\partial t} = \chi_c \Delta c - \gamma_c o c + c^+ \\ \frac{\partial o}{\partial t} = \alpha_0 \Delta o - \gamma_o b o + \delta_o (o^{max} - o) \\ \frac{\partial M}{\partial t} = -\beta_M M b \\ \frac{\partial A}{\partial t} = \gamma_A M b + \chi_{OA} \Delta A - \gamma_{OA} A \end{array} \right.$$

We have denoted the most sensitive variable that we will use in coupling and synchronization of the models, namely the tumor cells density  $b$ , by red color. We have also denoted the most sensitive model parameters, as found by the sensitivity analysis, by blue color.

The model is controlled by twenty-one parameters, presented in Table 1.

The tumor supermodel construction, as shown in Figure 4, involves:

- Homogenous tumor PDEs model, using the isogeometric alternating directions solver [12] and the embedded dynamic discrete vasculature graph [2].
- The sub-models are created based on either random selection of parameters, or they are pretrained with a genetic algorithm.
- In the second case, we use a simple genetic algorithm, finding local minima in the sensitive parameter space. The values of the parameters from these minima are selected to construct the three sub-models. We present more details in the numerical results section.
- The coupling of sub-models is performed based on a single dynamic variable, namely the tumor cell density.
- As ground truth, we use the results produced by a parallel multi-GPU tumor simulator. For more details regarding the simulator, we refer to Appendix A and [14].

Symbol	Value	Description
$b_m$	0	min tumor cell density
$b_M$	2	max tumor cell density
$b^{norm}$	1	normal tumor cell density
$D_b$	varies	tumor cell diffusion rate
$r_b$	0.3	tumor cells chemoattractant sensitivity
$\phi^{prol}$	10	tumor proliferation threshold
$\phi^{death}$	2	tumor cell hypoxia threshold
$T^{prol}$	10	tumor cell proliferation time
$T^{death}$	100	tumor cell survival time
$P_b$	0.001	maximum stimulated mitosis rate
$\tau_b$	0.5	instantaneous reaction rate
$\beta_M$	0.0625	ECM decay rate
$\gamma_A$	0.032	production rate of attractants
$\chi_{aA}$	0.000641	decay rate of digested ECM
$\gamma_{oA}$	0.000641	diffusion rate of digested ECM
$\chi_c$	0.0000555	TAF diffusion rate
$\gamma_c$	0.01	TAF decay rate
$\alpha_o$	0.0000555	oxygen diffusion rate
$\gamma_o$	0.01	oxygen consumption rate
$\delta_o$	0.4	oxygen delivery rate
$\phi^{max}$	60	maximal oxygen concentration

Table 1: Tumor model parameters [35].

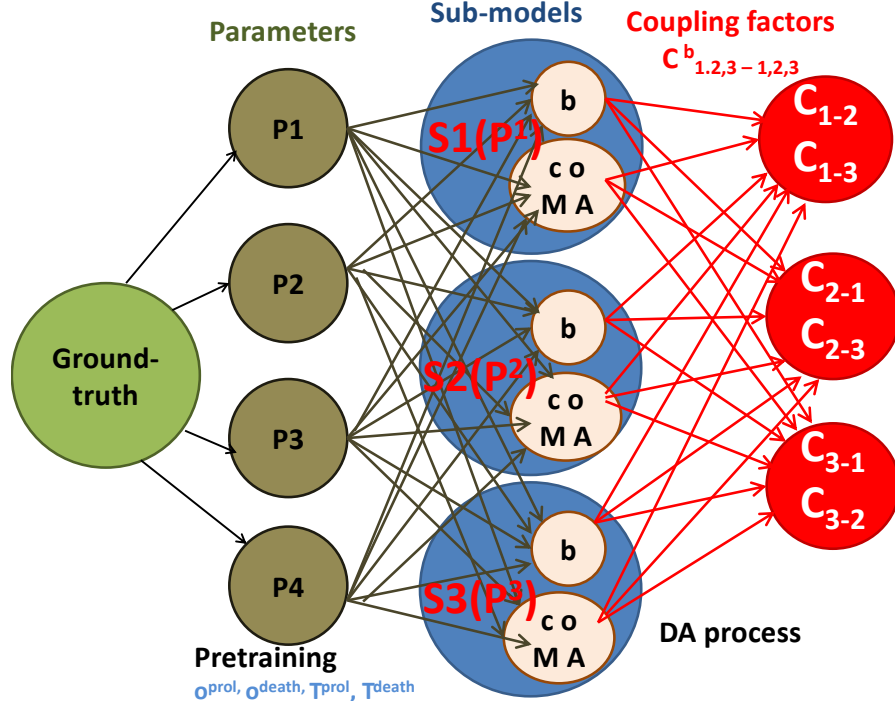


Figure 4: Dynamic variable used for coupling: tumor cell density  $b$  and most sensitive model parameters: tumor cell proliferation threshold  $o^{prol}$  and hypoxia threshold  $o^{death}$ , tumor cell proliferation time  $T^{prol}$  and survival time  $T^{death}$

#### 4. Sensitivity analysis

We first perform the tumor model sensitivity analysis.

We turned the IGA-ADS tumor solver to be a stand-alone code, executed with the input parameters provided from the command line, e.g.:

```
./tumor3d 4 12 2 120 300 1 0 2 1 0.3 10 2 10 100 0.001 0.5 0.0625 0.032
0.000641 0.000641 0.0000555 0.01 0.0000555 0.01 0.4 60
```

Where 4 corresponds to the number of nodes, 12 corresponds to the number of threads per node, 2 corresponds to the B-spline order  $p$ , 120 corresponds to the mesh size = the number of elements  $N_e$  in one direction (resulting in  $(N_e + p)^3 = 122^3 = 1,815,848$  unknown coefficients of the tumor density scalar field to couple in the supermodel), 300 corresponds to the number of time steps, 1 corresponds to the time step size (in the dimensionless form). Then we follow with all the model parameters like in Table 1.

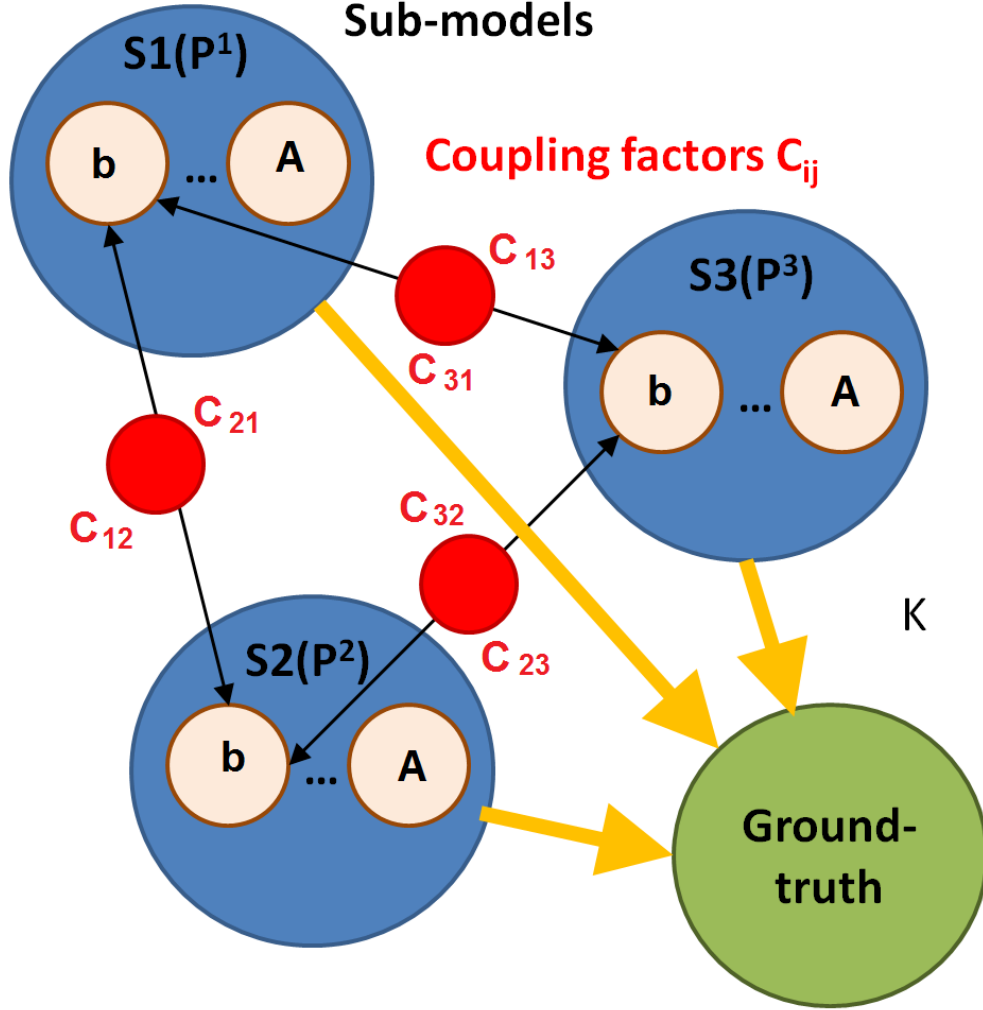


Figure 5: Supermodel as a coupling between three sub-models nudged to the Ground Truth.

The tumor cell diffusion rate  $D_b$  is fixed during the simulation since it is a property of the tissue.

We perform the sensitivity analysis of the model using the following method. We start with the above reference values of the parameters. We pick one parameter, and we run 20 simulations varying its values  $\pm 40$  percent with respect to the reference values while keeping other parameters fixed.



For example, possible modifications of parameter tumor proliferation threshold  $\phi^{prol}$  are

```
./tumor3d 4 12 2 120 300 1 0 2 1 0.3 6 2 10 100 0.001 0.5 0.0625 0.032
0.000641 0.000641 0.0000555 0.01 0.0000555 0.01 0.4 60
```

...

```
./tumor3d 4 12 2 120 300 1 0 2 1 0.3 10 2 10 100 0.001 0.5 0.0625 0.032
0.000641 0.000641 0.0000555 0.01 0.0000555 0.01 0.4 60
```

...

```
./tumor3d 4 12 2 120 300 1 0 2 1 0.3 14 2 10 100 0.001 0.5 0.0625 0.032
0.000641 0.000641 0.0000555 0.01 0.0000555 0.01 0.4 60
```

We find out that the model is most sensitive to the four parameters, denoted in Table 1 by blue color, namely tumor proliferation threshold, tumor cell hypoxia threshold, tumor cell proliferation time, tumor cell survival time.

The sensitivity analysis results for these four parameters are summarized in Figures 6-9.

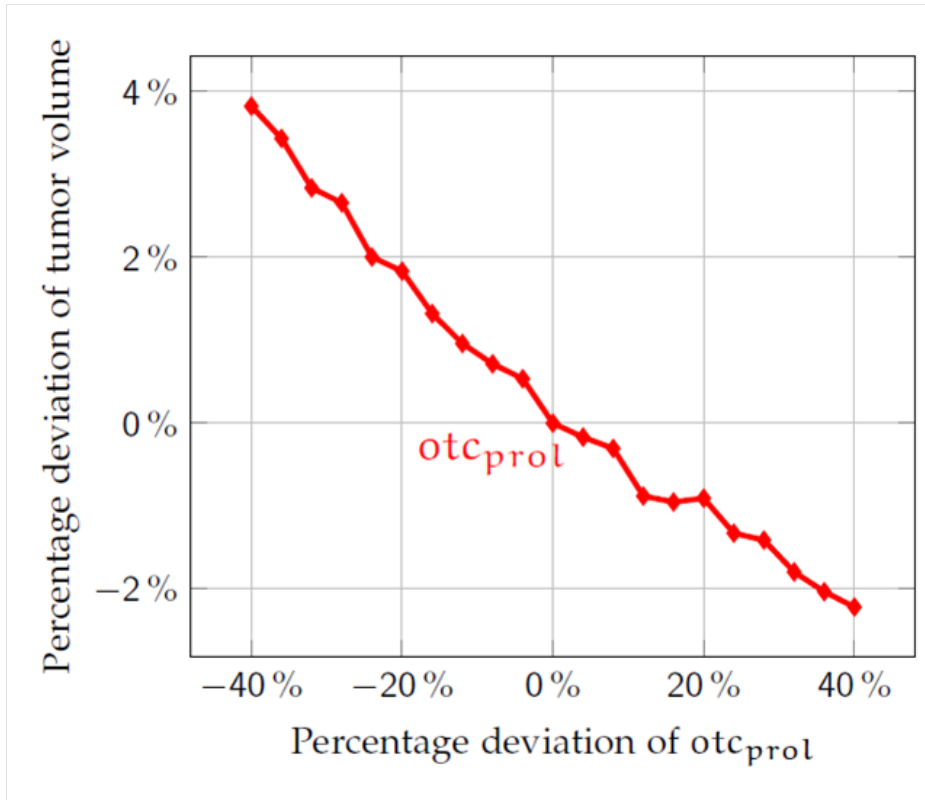


Figure 6: Sensitivity of the tumor model with respect to tumor proliferation threshold.

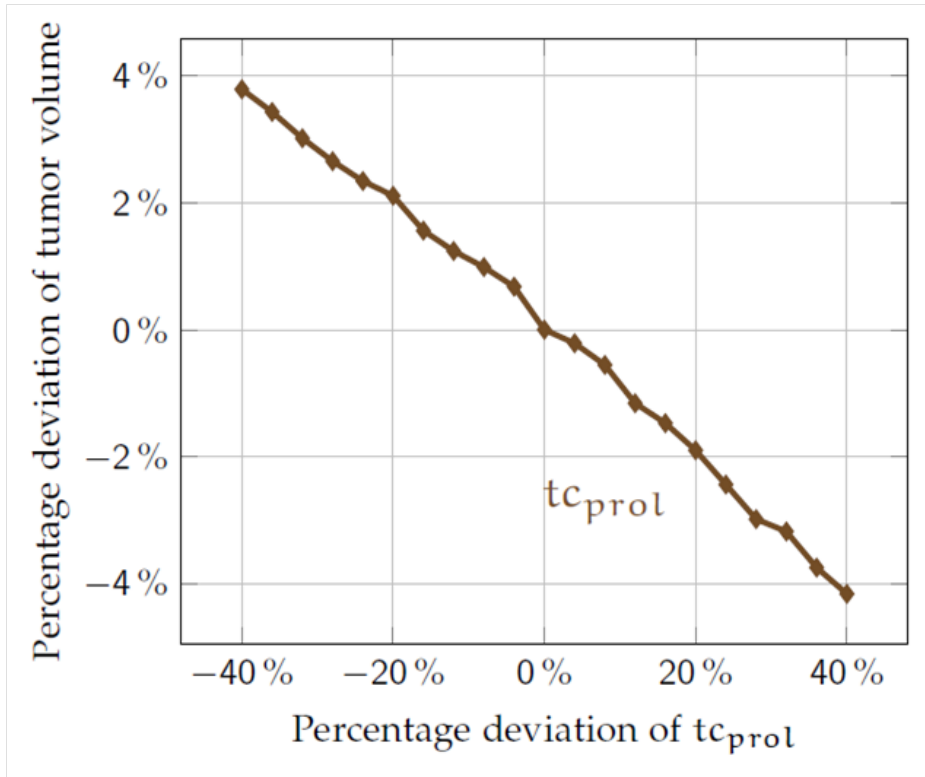


Figure 7: Sensitivity of the tumor model with respect to tumor cell proliferation time.

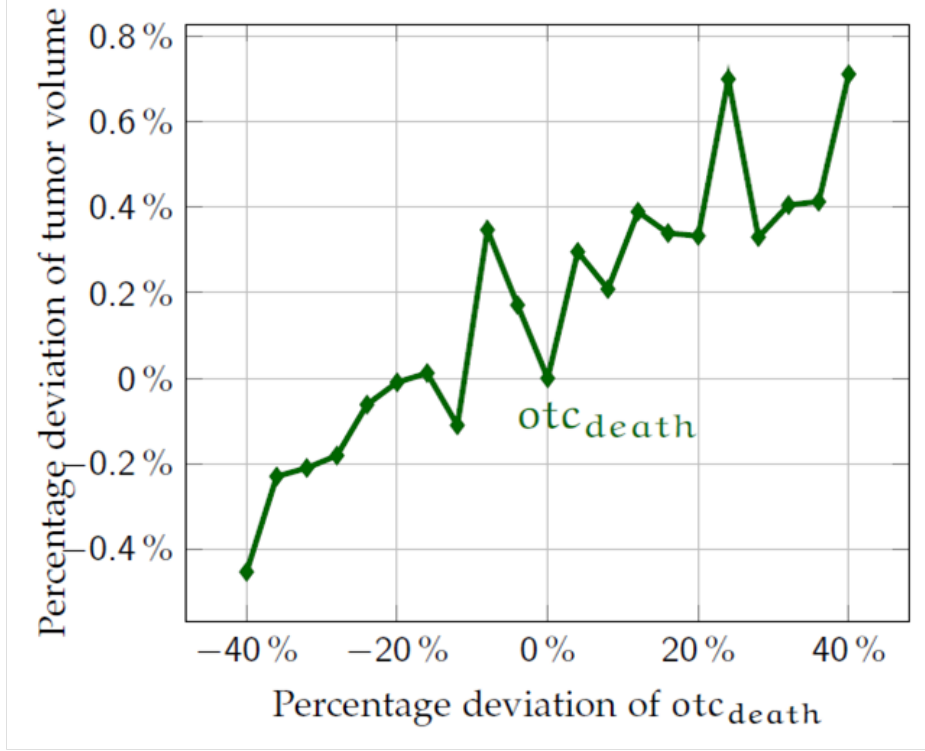


Figure 8: Sensitivity of the tumor model with respect to tumor cell hypoxia threshold.

## 5. Inverse problem solution with genetic algorithm

To find the values of the four most sensitive parameters that approximate the ground truth, we have executed the simple genetic algorithm [38]. In other words, each of the individuals in the initial genetic population has some randomly selected values of tumor proliferation threshold, tumor cell hypoxia threshold, tumor cell proliferation time, and tumor cell survival time. As the ground truth, we took some numerical results generated with the high fidelity model [14]. As the fitness function, we measure the total tumor volume. Namely, we sum up all the degrees of freedom for the tumor cells density, through the entire mesh, through all the time steps, and we compute the difference between the total tumor volume between the ground truth results and a simulation executed for a set of parameters stored by the individual in the genetic simulation:

$$\text{fitness}(GT, sim) = |\text{volume}(b^h) - \text{volume}(b^{GT})| \quad (12)$$

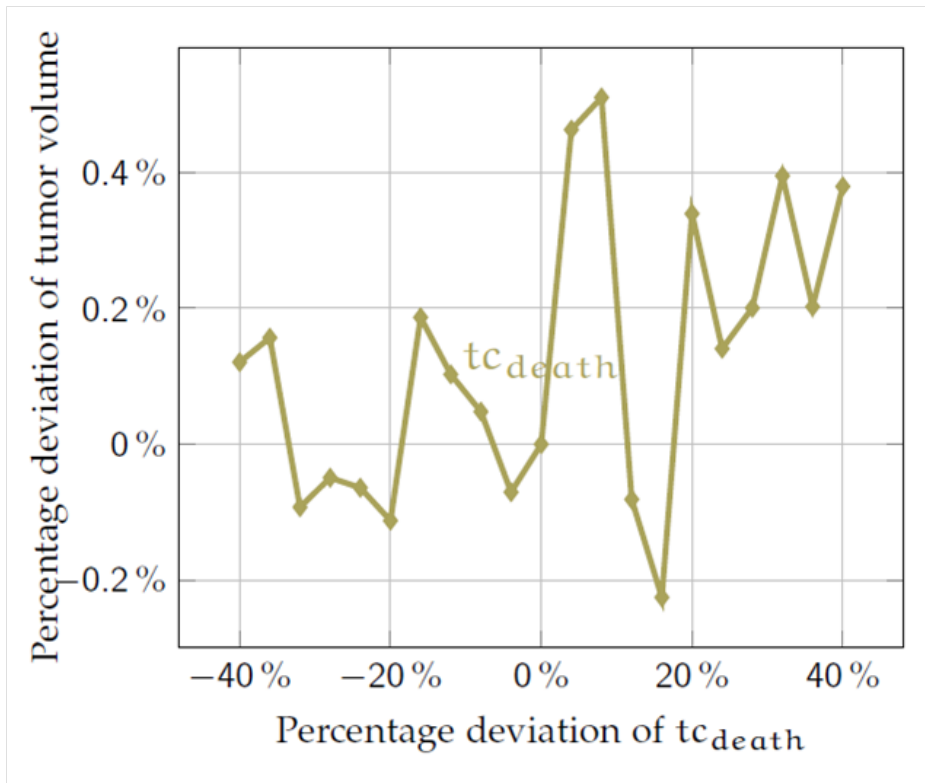


Figure 9: Sensitivity of the tumor model with respect to tumor cell survival time.

where

$$\begin{aligned} \text{volume}(b) &= \sum_{t=1}^T \int_{\Omega} b \, dx dy dz = \\ &\sum_{t=1, \dots, T} \sum_{i,j,k=1, \dots, (N_e+p)} b_{i,j,k}(t) \int_{\Omega} B_{i,p}^x(x) B_{j,p}^y(y) B_{k,p}^z(z) \end{aligned} \quad (13)$$

where  $b^h$  denotes numerical solution and  $b^{GT}$  corresponds to the total tumor volume as computed in the high fidelity model ground truth simulation.

For the computations of the volume we use the coefficients  $b_{i,j,k}(t)$  of B-splines of order  $p$  span over the computational mesh with  $N_e^3$  elements in each direction, in every time step  $t$ . Both the ground truth and the numerical solution in time moment  $t$  are represented as a linear combinations of B-splines span over the computational mesh. Namely, the numerical solution

$$b^h(x, y, z; t) = \sum_{i,j,k=1, \dots, (N_e+p)} b_{i,j,k}^h(t) B_{i,p}^x B_{j,p}^y B_{k,p}^z \quad (14)$$

and the Ground Truth (projected onto the computational mesh)

$$b^{GT}(x, y, z; t) = \sum_{i,j,k=1, \dots, (N_e+p)} b_{i,j,k}^{GT}(t) B_{i,p}^x B_{j,p}^y B_{k,p}^z. \quad (15)$$

We execute the genetic algorithm with randomly selected initial population, we crossover, mutate, and evaluate the individuals and observe the convergence of the algorithm to the solution.

The difference of the total tumor volume from the simulation and the ground truth in the first 21 generations of the genetic algorithm consisting of 20 individuals in each generation is presented in Figure 10. The horizontal axis denotes the percentage differences of total tumor volumes with respect to the ground truth, the vertical one shows the number of iteration, and each dot represents a single individual.

The convergence of the total tumor volume, represented by the average, minimum, and maximum values of the fitness function (12) are presented in Figure 11. We can see that the populations do not want to converge to a single solution; they rather scatter in the local minima.

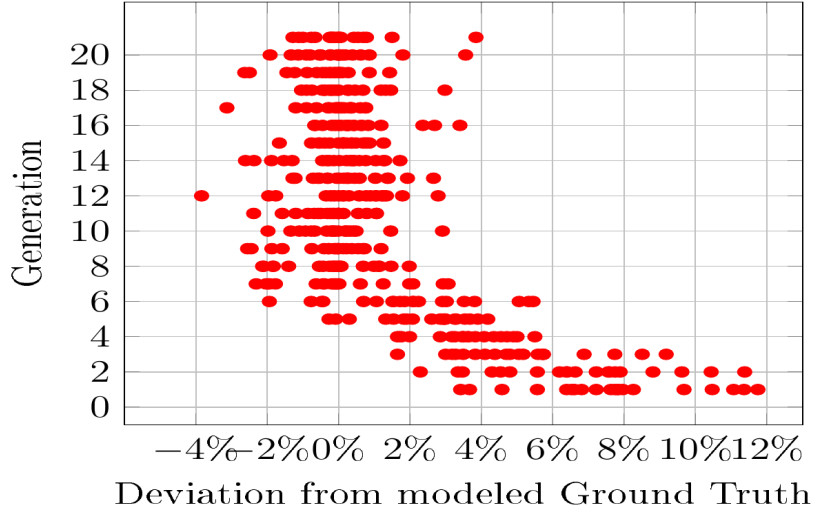


Figure 10: The populations of the genetic algorithm. The individuals in the population store the model parameters. The horizontal axis represents the differences of the tumor volume between the ground truth and the volumes resulting from running the simulation for particular individuals from the population. The vertical axis denotes the epochs of the genetic algorithm.

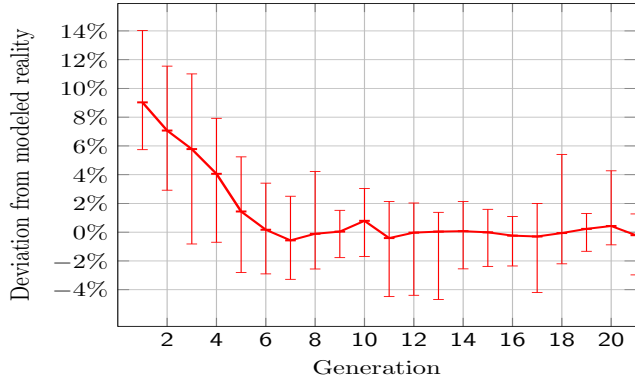


Figure 11: The convergence of the genetic algorithm.

## 6. Supermodeling algorithm

The supermodel is developed in three consecutive phases.

### 1. Initialization

- Perform sensitivity analysis to find the most sensitive parameters.

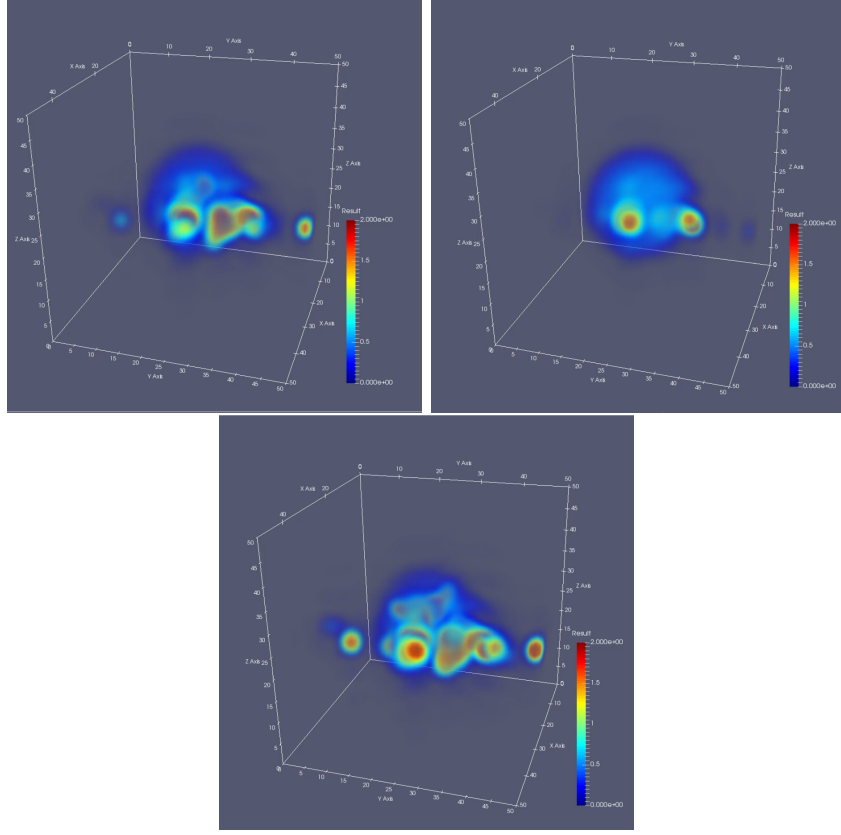


Figure 12: Tumor evolution simulations within three sub-models differing in parameters' values.

- Optionally solve the inverse problem to find local minima of the fitness function.
- Setup three sub-models:  $S_1$ ,  $S_2$  and  $S_3$  with different parameters' values, resulting in different tumor progressions, illustrated in Figure 12

## 2. Training

- Assume identical initial states in each sub-model,
- Setup coupling weights  $C_{ij}^b$  for  $i, j = 1, 2, 3$ , and  $K$  coefficient.
- For STEP=1,...,T



- (a) Run one simulation step in each submodel ( $S_1$ ,  $S_2$  and  $S_3$ ).
- (b) Modify obtained fields using the coupling constants

$$b^{h,i}(x, y, z; t) + = \sum_{j=1,2,3} C_{ij}^b (b^{h,j}(x, y, z; t) - b^{h,i}(x, y, z; t)) + K (b^{mean}(x, y, z; t) - b^{h,i}(x, y, z; t)). \quad (16)$$

where this correction is understood coefficient-wise, in a sense that these scalar fields are approximated as linear combinations of B-spline basis of order  $p$  span over the computational mesh with  $N_e$  elements. Namely,

$$b^{h,i}(x, y, z; t) = \sum_{m,n,o=1,\dots,(N_e+p)} b_{m,n,o}^{h,i}(t) B_{m,p}^x B_{n,p}^y B_{o,p}^z \quad (17)$$

where  $i$  is the sub-model index and  $m, n, o$  are indexes of its coefficients at time moment  $t$ , and we update it coefficient-wise at a given time moment  $t$

$$b_{m,n,o}^{h,i}(t) = \sum_{j=1,2,3} C_{ij}^b (b_{m,n,o}^{h,j}(t) - b_{m,n,o}^{h,i}(t)) + K (b_{m,n,o}^{mean}(t) - b_{m,n,o}^{h,i}(t)) \quad (18)$$

where

$$b_{m,n,o}^{mean}(t) = \frac{1}{3} \sum_{i=1,2,3} b_{m,n,o}^{h,i}(t) \quad (19)$$

- (c) Correct the coupling parameter:

$$C_{ij}^b + = \int_{\Omega} (b^{h,i}(x, y, z; t) - b^{mean}(x, y, z; t)) * (b^{h,i}(x, y, z; t) - b^{h,j}(x, y, z; t)) dx dy dz.$$

where the integral is computed over the cube-shape domain using the discrete combinations of B-spline basis functions representing the particular fields, and the mean field.

$$C_{ij}^b + = \sum_{m,n,o=1,\dots,(N_e+p)} (b_{m,n,o}^{h,i}(t) - b_{m,n,o}^{mean}(t)) *$$

$$\begin{aligned}
& \int_{\Omega} (B_{m,p}^x(x) B_{n,p}^y(y) B_{o,p}^z(z)) dx dy dz \\
& \sum_{m,n,o=1,\dots,(N_e+p)} (b_{m,n,o}^{h,i}(t) - b_{m,n,o}^{h,j}(t)) * \\
& \int_{\Omega} (B_{m,p}^x(x) B_{n,p}^y(y) B_{o,p}^z(z)) dx dy dz. \tag{20}
\end{aligned}$$

### 3. Supermodel simulation

- Setup identical initial states in each sub-model.
  - Use coupling weights  $C_{ij}^b$  for  $i, j = 1, 2, 3$ , and  $K$  coefficient as obtained from training stage.
  - For STEP=1,...,300
- (a) Run 1 step in each simulator (sim1, sim2, sim3).
  - (b) Modify obtained fields using the coupling constants

$$\begin{aligned}
& b^{h,i}(x, y, z; t) + = \\
& \sum_{j=1,2,3} C_{ij}^b (b^{h,j}(x, y, z; t) - b^{h,i}(x, y, z; t)) + \\
& K (b^{mean}(x, y, z; t) - b^{h,i}(x, y, z; t)) \tag{21}
\end{aligned}$$

which is performed coefficient-wise in every time moment  $t$

$$\begin{aligned}
& b_{m,n,o}^{h,i}(t) + = \\
& \sum_{j=1,2,3} C_{ij}^b (b_{m,n,o}^{h,j}(t) - b_{m,n,o}^{h,i}(t)) + \\
& K (b_{m,n,o}^{mean}(t) - b_{m,n,o}^{h,j}(t)) \tag{22}
\end{aligned}$$

## 7. Numerical results

We have performed several numerical experiments to verify the super-modeling approach. Below we demonstrate and discuss a summary of the selected three numerical experiments.

### 7.1. First experiment

In the first numerical experiment, we build three sub-models with randomly selected most sensitive parameters which values have been distributed as  $\pm 40\%$  around the reference values. We start the training phase with the coupling constants  $C_{ij} = 0.5$ , and the parameter coupling with the reality  $K = 2.0$ . We have set up the range of the  $C_{ij}$  values between  $[0.1, 0.9]$ .

We present in Figure 13 the dynamics of the coupling coefficients  $C_{ij}$  during training. We can see that they do not converge since they reach the minimum possible value of 0.1. The horizontal axis denotes the number of time steps, and the vertical axis indicates the values of the coefficients.

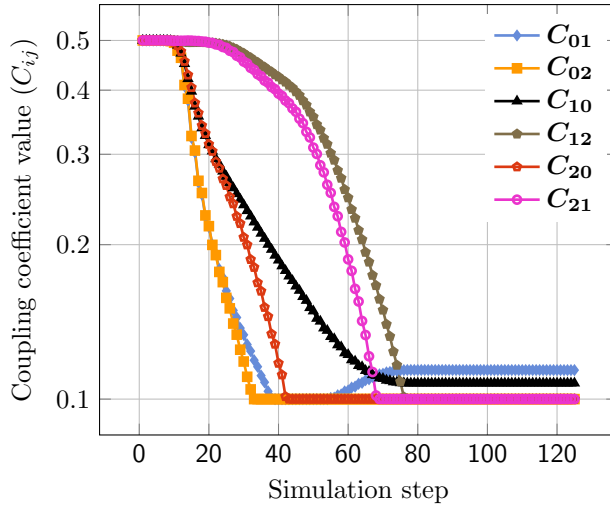


Figure 13: Convergence of coupling coefficients  $C_{ij}$  for  $K = 2.0$ .

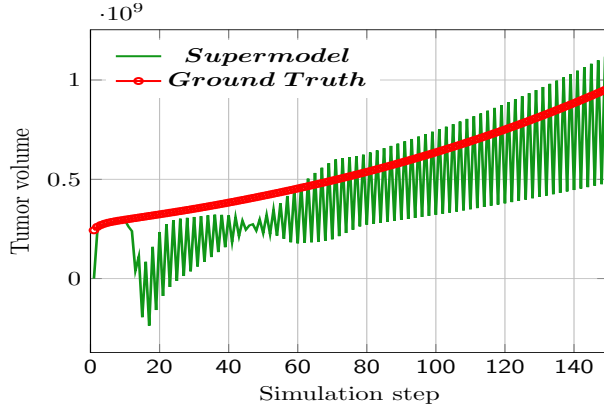


Figure 14: Convergence of tumor volumes for supermodel with respect to the Ground Truth.

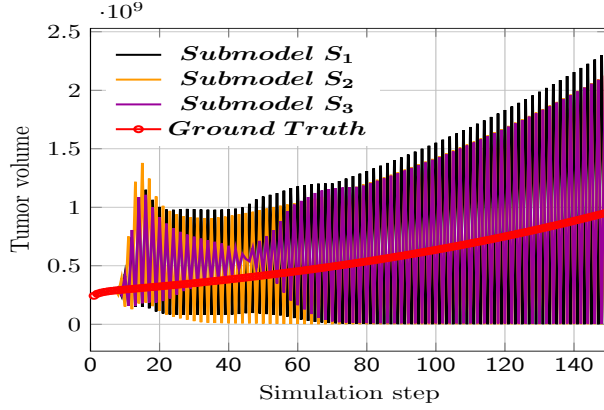


Figure 15: Convergence of tumor volumes for submodels with respect to the Ground Truth.

We investigate the problem further by presenting in Figures 14 and 15 the convergence of the supermodel to the ground truth, measured in terms of the total tumor volume. This time the horizontal axis denotes the number of time steps, and the vertical axis denotes the total tumor volumes. We present the volumes for particular sub-models (14), as well as for the average of the sub-models (15) and the ground truth simulation ("reality"). We can read from these figures that the sub-models and the supermodel fell into oscillations, and we find out that the reason is that our coefficient  $K$  coupling with the reality is too big, generating numerical oscillations.

Total tumor volume (presented in Figure 14) consists of the volume of proliferating and quiescent cells. Proliferating cells are those who multiply due to the high local concentration of the oxygen. The quiescent tumor cells are the cells which cannot proliferate due to unfavorable living conditions such as hypoxia or the high pressure (e.g., [34]). Next, we present the supermodel's convergence to the ground truth, measured in terms of the proliferating tumor cells. As previously we present the volumes of proliferating cells for particular sub-models (17), as well as for the average of the sub-models (16) and the ground truth ("reality").

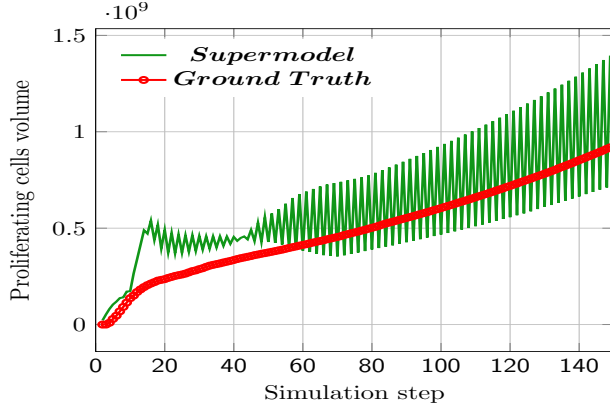


Figure 16: Convergence of the volumes of tumor proliferating cells for supermodel with respect to the Ground Truth.

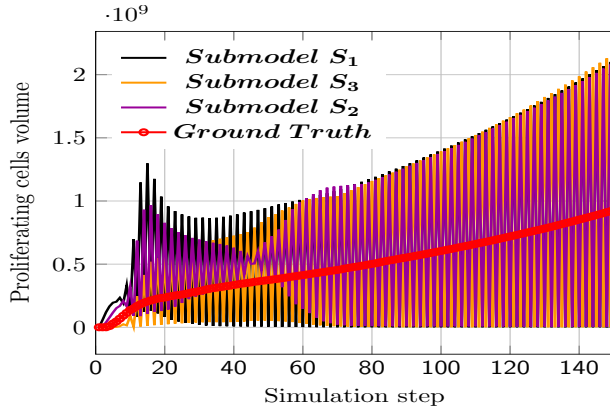


Figure 17: Convergence of the volumes of tumor proliferating cells for submodels with respect to the Ground Truth.

Next, in Figures 18 and 19 we present the convergence of the supermodel to the ground truth, this time measured in terms of the quiescent tumor cells. We present the volumes of quiescent cells for particular sub-models (19), for the average of the sub-models (18), and for the ground truth.

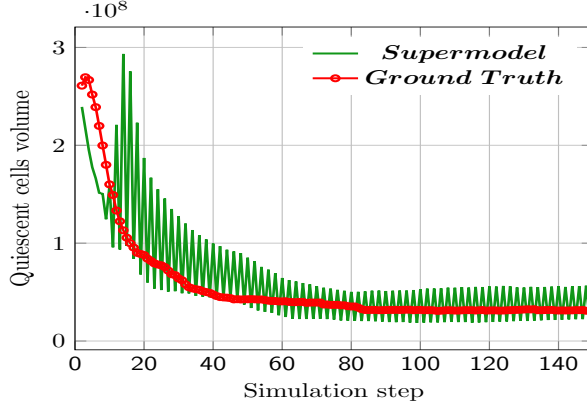


Figure 18: Convergence of the volumes of tumor quiescent cells for supermodel with respect to the Ground Truth.

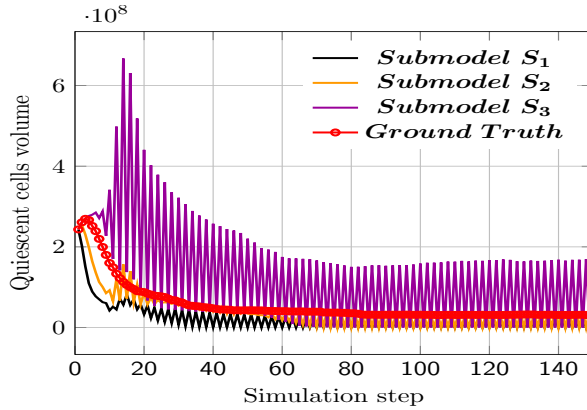


Figure 19: Convergence of the volumes of tumor quiescent cells for submodels with respect to the Ground Truth.

Finally, in Figure 20 we present the difference between supermodel with respect to the Ground Truth, for the supermodel before and after the training phase.

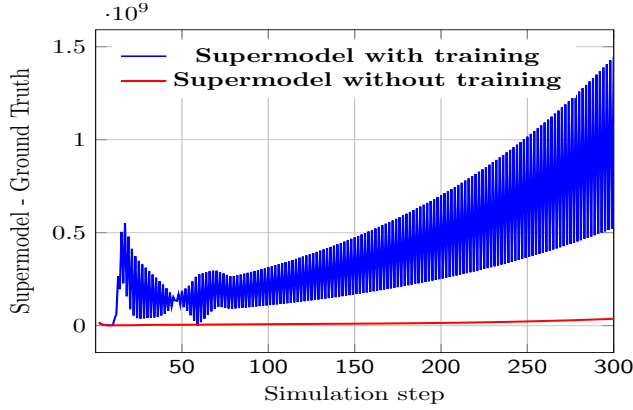


Figure 20: Difference between supermodel with respect to the Ground Truth, for the supermodel before and after the training phase.

All presented figures confirms that in given configuration (i.e. with  $K = 2.0$ ) supermodeling does not work and, as mentioned, the reason is too high value of the  $K$  coefficient what results in numerical oscillations.

### 7.2. Second experiment

In the second experiment, we also build three sub-models with randomly selected most sensitive parameters which values have been distributed as  $\pm 40\%$  around the reference values. We start the training phase with the coupling constants  $C_{ij} = 0.5$ . We allow them to vary in the range of  $[0.1, 0.9]$ . This time we set the value of the  $K$  parameter to  $K = 0.9$ . Now, we expect much better results (and their stabilization).

In Figure 21 we demonstrate that the coupling coefficients  $C_{ij}$  converge indeed to the reasonable value.

In Figures 22 and 23, we present the convergence of the supermodel and its sub-models to the ground truth. We measure the convergence in terms of the total tumor volume. We present the volumes for particular sub-models (Figure 23), for the average of the sub-models (Figure 22) and for the ground truth.

Again, since total tumor volume (presented in Figure 22) consists of the volume of proliferating and quiescent cells – to give a better overview what is happening inside the model in Figures 24 and 25 we present the convergence of the supermodel to the ground truth, measured in terms of the proliferating tumor cells. As previously we present the volumes of proliferating cells for

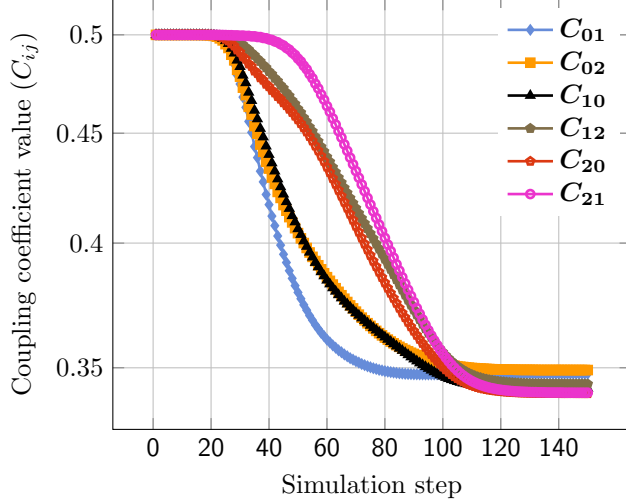


Figure 21: Convergence of coupling coefficients  $C_{ij}$  for  $K = 0.9$ .

particular sub-models (25), as well as for the average of the sub-models (24) and the ground truth ("reality").

Next, in Figures 26 and 27 we present the convergence of the supermodel to the ground truth, this time measured in terms of the quiescent tumor cells. We present the volumes of quiescent cells for particular sub-models (27), for the average of the sub-models (26) and for the ground truth.

Finally, in Figure 28 we present the difference of the total tumor volume and the ground truth, for the supermodel executed without the training phase (all  $C_{ij} = 0.5$ ), and after the training.

We can see the improvement of the convergence, but there is still quite a difference between the supermodel and the ground truth. To improve the supermodel, we will employ the genetic algorithm to find local minima and then we will build sub-models based on the parameters located in the local minima.

### 7.3. Third experiment

In the third numerical experiment, we build three sub-models from the parameters coming from the best-fitted individuals, as found by the genetic algorithm. We start the training phase with the coupling constants  $C_{ij} = 0.5$ , and the parameter coupling with the reality  $K = 0.9$ . We set up the range of the  $C_{ij}$  values between  $[0.1, 0.9]$ .

In Figure 29 we present the convergence of the coupling coefficients  $C_{ij}$ .



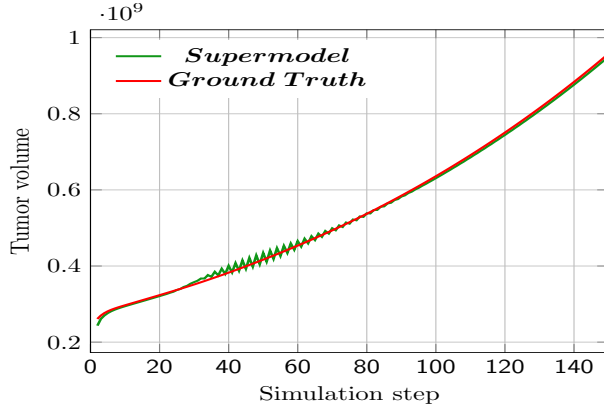


Figure 22: Convergence of tumor volumes for supermodel with respect to ground truth.

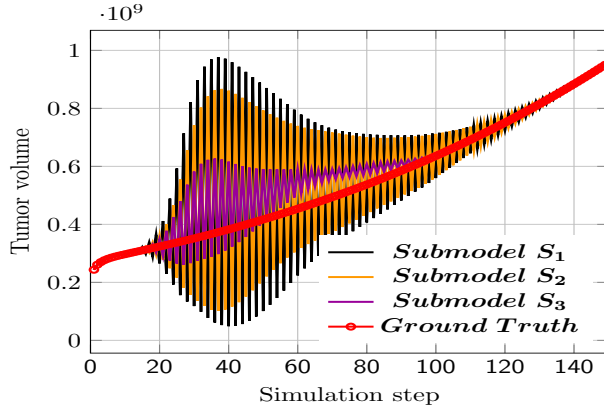


Figure 23: Convergence of tumor volumes for submodels with respect to ground truth.

In Figures 30 and 31, we present the convergence of the supermodel and its sub-models to the ground truth. We measured the convergence in terms of the total tumor volume. We present the volumes for particular sub-models (Figure 31), the average of the sub-models (Figure 30) and the ground truth simulation.

Again, to give a better overview what is happening in the model, in Figures 32–35 we present the convergence of the supermodel and submodels. We measure the convergence in terms of the proliferation and quiescent tumor cells volume.

Finally, in Figure 36 we present the difference of the total tumor volume with respect to the ground truth, for the supermodel executed without the

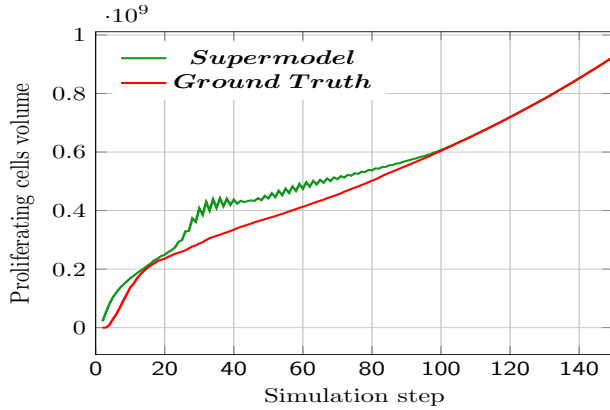


Figure 24: Convergence of the volumes of tumor proliferating cells for supermodel with respect to the ground truth.

training phase (all  $C_{ij} = 0.5$ ), and after the training.

From the numerical results, we can see that both randomly selected supermodels, with proper distribution of parameters and the sub-models generated by the simple genetic algorithm, deliver a similar good quality of the sub-model. In the following part of the paper, we select different numbers of submodels and different initial distribution of submodels. We test their dependence on the convergence of the training procedure and the quality of the resulting supermodel.

#### 7.4. Dependency on the number of submodels and initial parameter distribution

In Figure 3 we presented two different "localizations" of submodels with respect to the ground-truth. In the first case presented schematically in Figure 3a, the submodels "surround" ground-truth, which, as we expect, can be approximated by the linear combination of sub-models. In the second case, presented in Figure 3b we do not have such a situation since all submodels are 'located' to the left of the ground-truth and we expect that in such case approximation of reality through a linear combination of submodels will be less effective than in the first case. We investigated this aspect performing some experiments where we initially dispersed submodels parameters in three different ways, i.e.

- parameters of submodels have been distributed evenly around the reference value. For instance, assuming that the reference value of  $\sigma^{prol}$

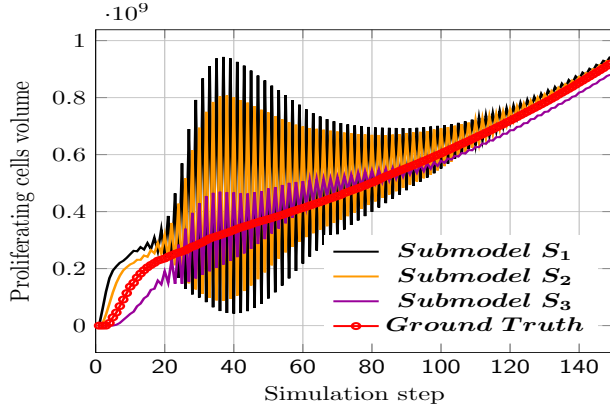


Figure 25: Convergence of the volumes of tumor proliferating cells for submodels with respect to the Ground Truth.

is 10 we created submodels where in some of them the value of this parameter has been greater than this value and in the rest it has been less than the reference value.

- parameters of submodels have been distributed "below" the reference value. For instance, assuming that the reference value of  $\sigma^{prol}$  is 10 we created submodels where in all of them the value of this parameter has been less than the reference value.
- parameters of submodels have been distributed "above" the reference value. For instance, assuming that the reference value of  $\sigma^{prol}$  is 10 we created submodels where in all of them the value of this parameter has been greater than the reference value.

In Figures 37-39 we present some exemplary results. We present results for three supermodels consisting of six, seven, and eight submodels, respectively. We want to answer the question of how much the supermodel's efficiency depends on the number of submodels. For experiments with six submodels, we took the following configurations:

- `./tumor_3d 4 2 10 32 300 6 9.0 3.0 5.0 7.0 11.0 15.0` what means that we run a supermodel consisting of six submodels. In three of submodels the  $\sigma^{prol}$  parameter value has been set to 5.0, 7.0 and 9.0 (i.e., below the reference value). The other three of the submodels have this parameter set to 11.0 13.0 and 15.0, respectively (above the reference value)

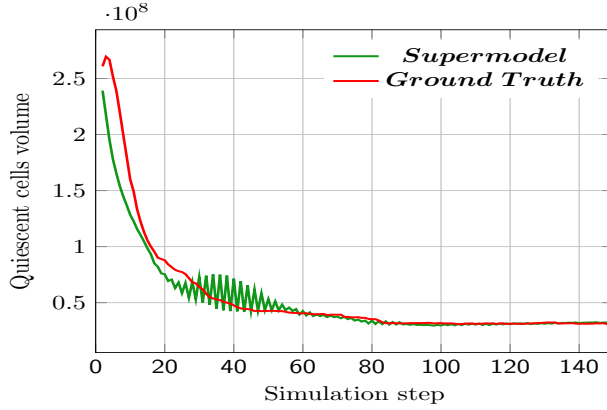


Figure 26: Convergence of the volumes of tumor quiescent cells for supermodel with respect to the ground truth.

- `./tumor_3d 4 2 10 32 300 6 9.0 4.0 5.0 6.0 7.0 8.0` what means that we run supermodel consisting of six submodels, where in all submodels the  $\sigma^{prol}$  parameter has the value below the reference value of this parameter (i.e. 4.0, 5.0, 6.0, 7.0, 8.0 and 9.0 respectively)
- `./tumor_3d 4 2 10 32 300 6 11.0 12.0 13.0 14.0 15.0 16.0` what means that we run supermodel consisting of six submodels, where in all submodels the  $\sigma^{prol}$  parameter has the value above its reference value (i.e. 11.0, 12.0, 13.0, 14.0, 15.0 and 16.0 respectively)

Similarly, for experiments with seven submodels, we took the following configurations:

- `./tumor_3d 4 2 10 32 300 7 3.0 5.0 7.0 9.0 11.0 13.0 15.0` what means that we run a supermodel consisting of seven submodels. In four of submodels the  $\sigma^{prol}$  parameter value has been set to 3.0, 5.0, 7.0 and 9.0 (i.e., below the reference value). In the other three submodels this parameter has values of 11.0 13.0 and 15.0, respectively (above the reference value)
- `./tumor_3d 4 2 10 32 300 7 3.0 4.0 5.0 6.0 7.0 8.0 9.0` what means that we run supermodel consisting of six submodels where in all submodels the  $\sigma^{prol}$  parameter has the value below the reference value of this parameter (i.e., 3.0, 4.0, 5.0, 6.0, 7.0, 8.0 and 9.0 respectively)

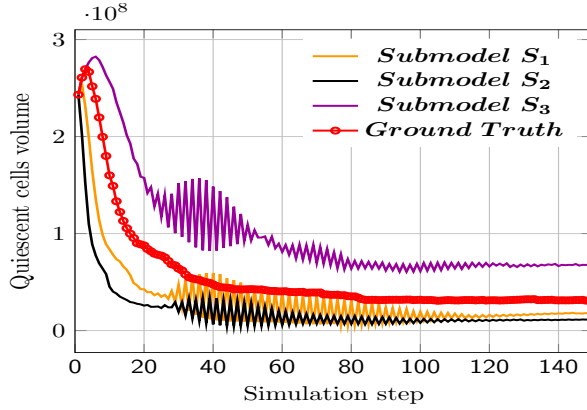


Figure 27: Convergence of the volumes of tumor quiescent cells for submodels with respect to the ground truth.

- `./tumor_3d 4 2 10 32 300 7 11.0 12.0 13.0 14.0 15.0 16.0 17.0` what means that we run supermodel consisting of seven submodels, where in all submodels the  $\sigma^{prol}$  parameter has the value above its reference value (i.e. 11.0, 12.0, 13.0, 14.0, 15.0, 16.0 and 17.0 respectively).

Finally, for experiments with eight submodels, we took the following configurations:

- `./tumor_3d 4 2 10 32 300 8 3.0 5.0 7.0 9.0 11.0 13.0 15.0 17.0` what means that we run supermodel consisting of seven submodels. In four of submodels the  $\sigma^{prol}$  parameter value has been set to 3.0, 5.0, 7.0 and 9.0 (i.e., below the reference value). In the other submodels this parameter has been set to 11.0, 13.0, 15.0 and 17.0, respectively (above the reference value)
- `./tumor_3d 4 2 10 32 300 8 2.0 3.0 4.0 5.0 6.0 7.0 8.0 9.0` what means that we run supermodel consisting of six submodels. In all submodels the  $\sigma^{prol}$  parameter has the value below the reference value of this parameter (i.e. 3.0, 4.0, 5.0, 6.0, 7.0, 8.0 and 9.0 respectively)
- `./tumor_3d 4 2 10 32 300 8 11.0 12.0 13.0 14.0 15.0 16.0 17.0 18.0` what means that we run supermodel consisting of seven submodels. In all submodels the  $\sigma^{prol}$  parameter has the value above its reference value (i.e. 10.0, 11.0, 12.0, 13.0, 14.0, 15.0 and 16.0 respectively).

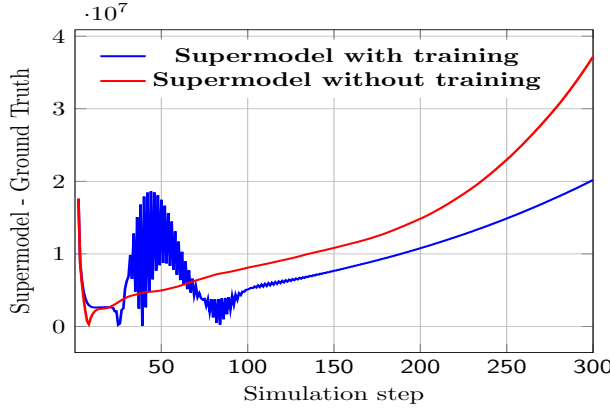


Figure 28: Difference between supermodel with respect to the Ground Truth, for the supermodel before and after the training phase.

In Figure 3, we formulated and visualized the intuition according to which the linear combination of supermodels where parameters surround corresponding reference values approximates the ground-truth better than in the case where submodels' parameters 'drift' in one direction in respect to corresponding reference values. As one may see, in all three presented cases, this intuition is confirmed since the black lines representing the submodels with parameter values surrounding reference values oscillate the most around zero. There is one more conclusion coming from Figures 37-39 i.e., along with the growing number of submodels, the better and faster is the convergence of the supermodel to the ground-truth.

#### 7.5. *Disturbance of insensitive parameters*

Another interesting issue is the behavior of the supermodel when in the initial stage, the values of not only (most) sensitive parameters are disturbed but also (all) others. One could assume the hypothesis that in the experiments presented so far, the supermodel was able to approximate reality because the parameter we have dispersed initially was the parameter on which the model is most sensitive. Consequently, in the supermodeling process, it is relatively easy to "correct" and adjust the model to reality because the model moderately "easily" responds to the correction of such a sensitive parameter. We repeat the experiments discussed section 7.2. This time we disturb all the parameters of the model except for `o_prol_tc`. The model is most sensitive with respect to this parameter, and it was disturbed in section 7.2. The disturbance of parameters was carried out in three variants -

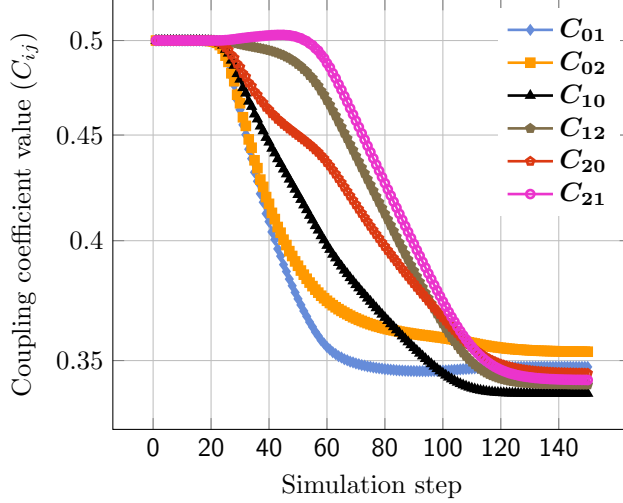


Figure 29: Convergence of coupling coefficients  $C_{ij}$  for  $K = 0.9$  with changed GT.

let's call them Variant I, Variant II and Variant III, whereas the disturbance parameter scheme presented in section 7.2 will be called Variant 0. In Variant I, all parameters (except  $o_{prol\_tc}$ ) were disturbed "around" the reference values (i.e. those presented in the Table 1) with a deviation of  $\pm 10\%$  from these reference values. In Variant II, all parameters (except  $o_{prol\_tc}$ ) were disturbed "around" the reference values (i.e. those presented in the Table 1) with a deviation of  $\pm 30\%$  from these reference values. Finally, in the Variant III, various schemes for distributing their parameters were used for individual sub-models. And so, for the first submodel all its parameters (except  $o_{prol\_tc}$ ) were scattered around the reference values with a deviation of  $\pm 10\%$ , for the second submodel all its parameters were scattered "below" the reference values in the range of:  $[ref - 20\%ref, ref - 10\%ref]$ , while for the third submodel all its parameters were scattered "above" reference values in the range of  $[ref + 10\%ref, ref + 20\%ref]$ .

As one may see in charts presented in Figure 40 for all three additional parameters disturbance schemes, the supermodel was able to converge towards the ground truth, but this time it took a little bit longer than for Variant 0. It seems to be very natural and intuitive. Since, this time, we disturbed less sensitive parameters, the model "reacts" slower on any changes of their values. The most similar to Variant 0 is Variant I – what seems natural

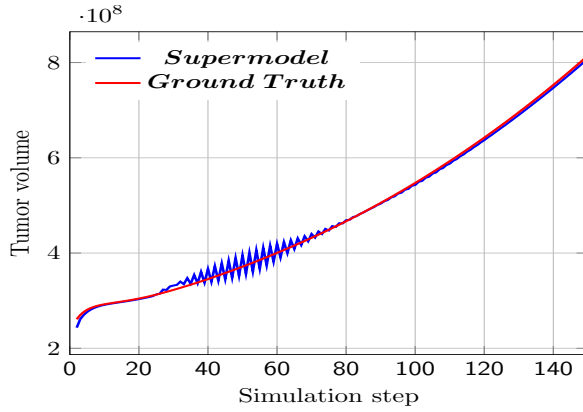


Figure 30: Convergence of tumor volumes for supermodel with respect to the Ground Truth.

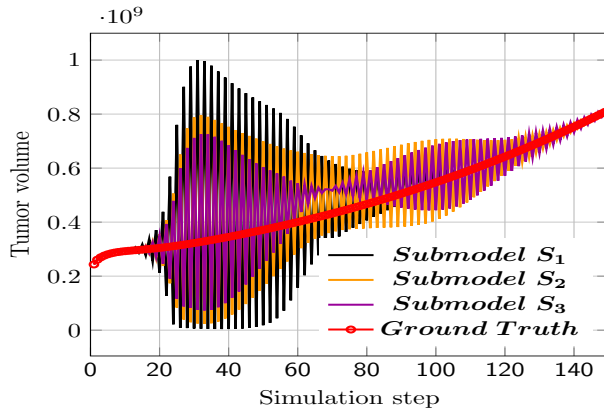


Figure 31: Convergence of tumor volumes for submodels with respect to the Ground Truth.

since in Variant I we used the smallest parameters values disturbance so the 'starting point' in Variant I is very close to those of Variant 0. The situation is slightly different for Variant II and III - in those cases, the supermodel can converge to the ground truth, but this time it takes a little longer. It also seems to be natural and in accordance with the intuition. Since the range of parameters disturbance is now greater, so at the beginning, the submodels are further from the ground truth it takes the supermodel more time to find out the 'reality'.



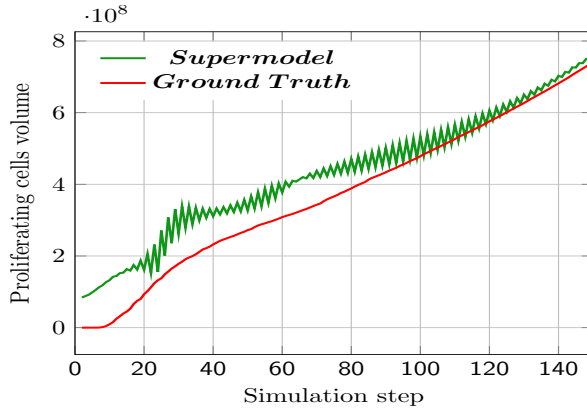


Figure 32: Convergence of the volumes of tumor proliferating cells for supermodel with respect to the Ground Truth.

## 8. Conclusions

We focused on the three-dimensional tumor growth model described by a system of PDEs with over 20 parameters. We simulated the tumor growth using a linear computational cost  $\mathcal{O}(N)$  alternating-direction isogeometric solver. We coupled the continuous model with a discrete vasculature graph. We performed the sensitivity analysis of the model, as well as the inverse simulation using a simple genetic algorithm. We found sets of model parameters that match the ground truth in the best way. As the ground truth, we use a high fidelity model executed on a GPU cluster. We found out that the inverse problem solutions fit into local minima, and an additional data assimilation process is necessary. We proposed the supermodeling approach for intelligent coupling and synchronization of several sub-models. We trained the coupling coefficients  $C_{ij}$ , and build the supermodel with three sub-models using the sets of parameters resulting from the inverse analysis. The supermodel matches well the ground truth data. A good agreement of the supermodel with "reality" is possible when proper training coefficient  $K$  is selected and when we have a good selection of sub-models, surrounding the ground truth. The future work will involve the construction of a supermodel with sub-models using different PDEs and different simulators.

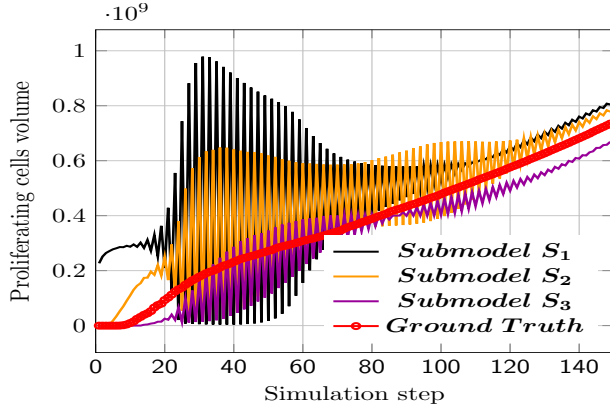


Figure 33: Convergence of the volumes of tumor proliferating cells for submodels with respect to the Ground Truth.

## 9. Acknowledgement

The work has been supported by Polish National Science Centre, Poland grant no. 2016/ 21/B/ST6/01539 and in part by PL-Grid Infrastructure. The visit of Maciej Paszyński at Oden Institute, The University of Texas at Austin, USA has been supported by J. T. Oden Research Faculty Fellowship.

## Appendix A. Parallel three-dimensional tumor simulator development for a cluster of GPUs

The solver performance is crucial from the point of view of practical applications of the supermodeling. The IGA solver discussed here was originally implemented in C++ and run on CPUs. Decomposition of calculations into threads and running computations on powerful supercomputers allowed to increase efficiency, however, in practical applications, it was still not enough, and the natural approach for further (significant) increasing the performance of this solver was to implement and run calculations on GPUs.

The algorithm of the isogeometric solver is shown in the Listing 1 below.

```
void simulation_base::run() {
    before();
    for (int i=0; i<steps.step_count; ++i) {
        before_step();
        step();
    }
```

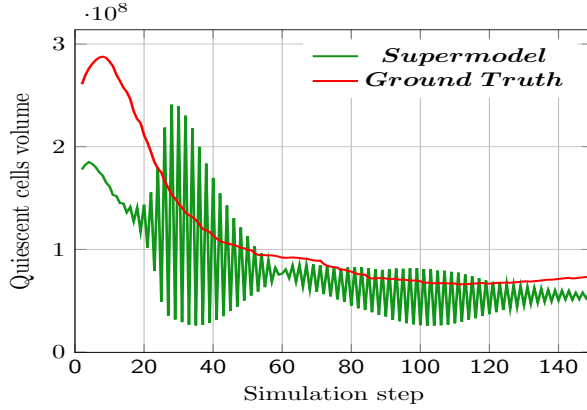


Figure 34: Convergence of the volumes of tumor quiescent cells for supermodel with respect to the Ground Truth.

```

    after_step();
}
after();
}

void step() override {
    compute_rhs();
    solve(u);
}

```

Listing 1: The algorithm of the isogeometric differential equations solver

At the start of the simulation, the solver performs pre-initialization in the *before()* function, and during multiple iterations of the *for* loop determines the subsequent states in consecutive time steps.

Running the next *step()* means calculating the right-hand side of the differential equation and calculating the solution by calling *solve(u)* function.

Before and after each call of the *step()* function, *before\_step()* and *after\_step()* are executed, where, among the others, matrix replacement and saving to the file of the currently calculated time step take place.

From the point of view of computational complexity, the computation time is 'consumed' mainly by *compute\_rhs()* (and *solve(u)*) functions appearing in the *step()* function, where the execution of the *compute\_rhs()* function 'consumes' over 99% of time in simulations with reasonable mesh sizes.

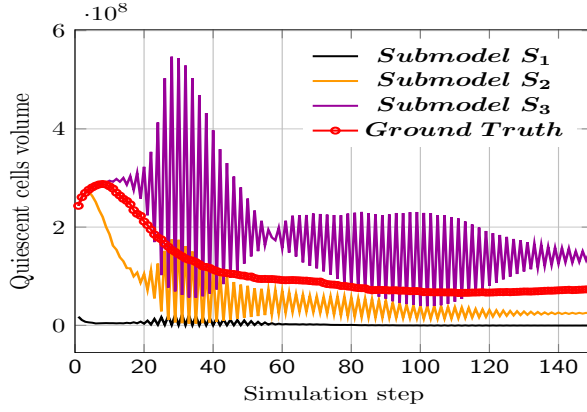


Figure 35: Convergence of the volumes of tumor quiescent cells for submodels with respect to the Ground Truth.

```

void compute_rhs(auto& rhs){
    executor.for_each(elements(), [&](index_type e){
        auto U = element_rhs();
        float J = jacobian(e);
        for (auto q : quad_points()){
            double w = weigth(q);
            value_type u = eval_fun(u_prev, e, q);
            for (auto a : dofs_on_element(e)){
                auto aa = dof_global_to_local(e, a);
                value_type v = eval_basis(e, q, a);
                float gradient_prod = grad_dot(u, v);
                float val = u.val * v.val - dt * gradient_prod;
                U(aa[0], aa[1]) += val * w * J;
            }
        }
    })
    executor.synchronized([&]() {
        update_global_rhs(rhs, U, e);
    });
}

```

Listing 2: Original CPU C++ IGA solver implementation

```

void compute_rhs(auto& rhs){

```

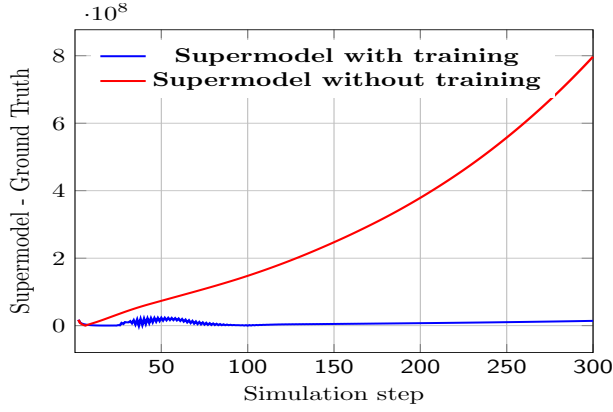


Figure 36: Difference between supermodel with respect to the Ground Truth, for the supermodel before and after the training phase.

```

executor.for_each(dofs(), [&](index_type a){
for (auto e : elements_supporting_dof(a)) {
    float J = jacobian(e);
    for (auto q : quad_points()){
        double w = weight(q);
        value_type u = eval_fun(u_prev, e, q);
        value_type v = eval_basis(e, q, a);
        float gradient_prod = grad_dot(u, v);
        float val = u.val * v.val - dt * gradient_prod;
        rhs(aa[0], aa[1]) += val * w * J;
    }
}
)}

value_type eval_fun(vector_type& v, index_type e,
    index_type q){
    value_type u{};
    for (auto b : dofs_on_element(e)) {
        float c = v(b[0], b[1]);
        value_type B = eval_basis(e, q, b); u += c * B;
    }
return u;
}

```

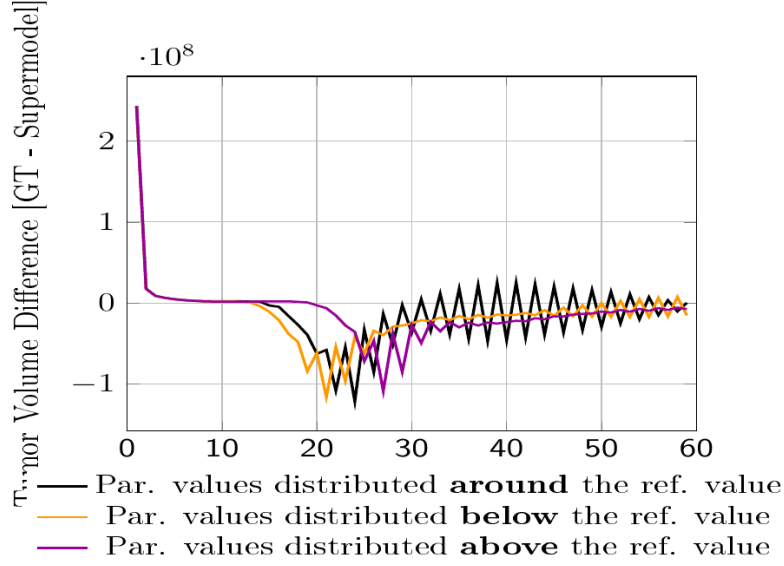


Figure 37: Difference between Ground Truth and supermodel predicted tumor volume for super model consisting of 6 submodels and with different starting parameter values distributions.

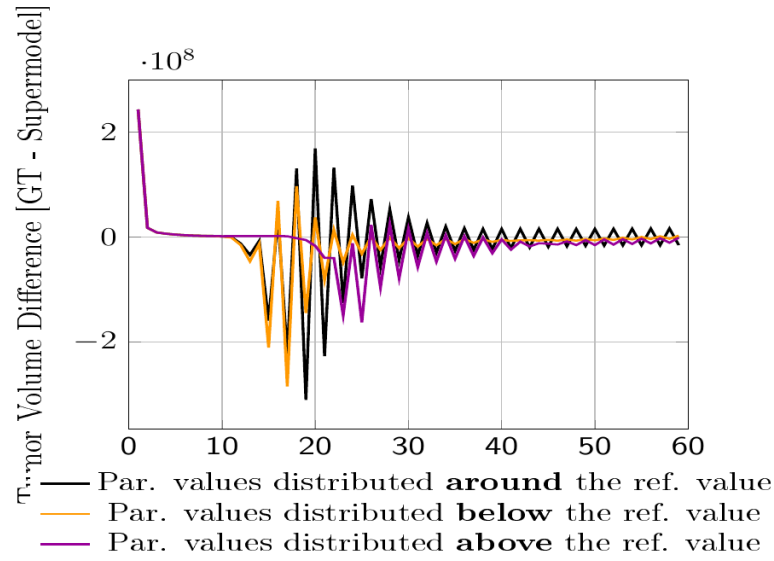


Figure 38: Difference between Ground Truth and supermodel predicted tumor volume for super model consisting of 7 submodels and with different starting parameter values distributions.

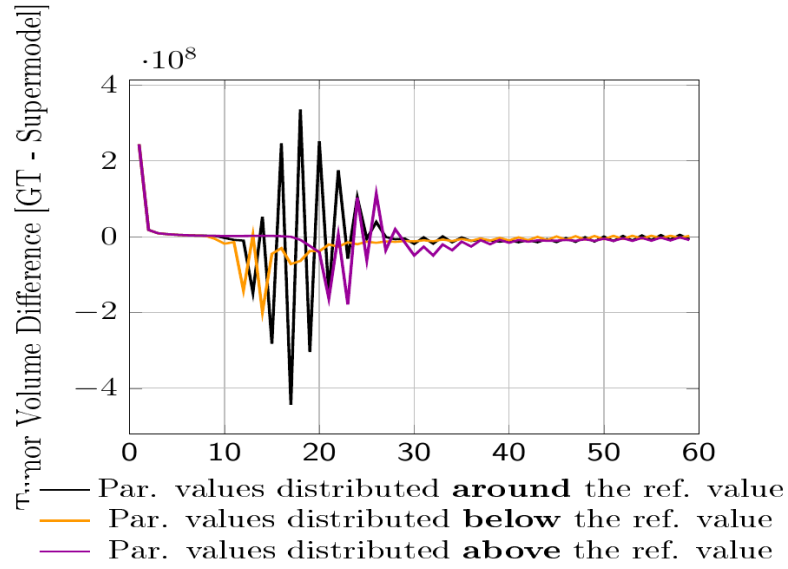


Figure 39: The difference between Ground Truth and supermodel predicted tumor volume for super model consisting of 8 submodels and with different starting parameter values distributions.

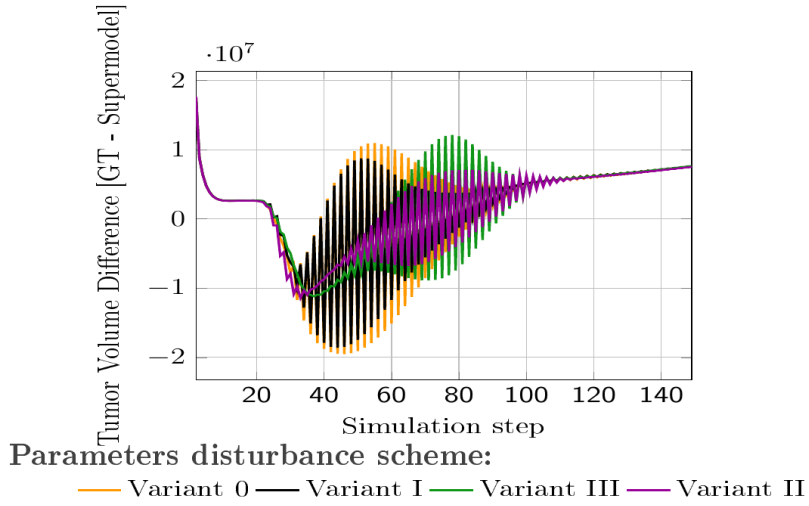


Figure 40: Comparison of supermodel convergence for different initial (insensitive) parameter disturbance schemes for  $K = 0.9$

```
}
```

Listing 3: Improved CPU C++ IGA solver implementation

```

void compute_rhs_prev(auto& rhs){
    executor.for_each(elements(), [&](index_type e){
        for (auto q : quad_points()){
            value_type u = eval_fun(u_prev, e, q);
            TMP_U_eval_fun[e][q] = u;
        }
    })
}

void compute_rhs_post(auto& rhs){
    executor.for_each(dofs(), [&](index_type a){
        for (auto e : elements_supporting_dof(a)) {
            float J = jacobian(e);
            for (auto q : quad_points()){
                double w = weigth(q);
                value_type u = TMP_U_eval_fun[e][q];
                value_type v = eval_basis(e, q, a);
                float gradient_prod = grad_dot(u, v);
                float val = u.val * v.val - dt * gradient_prod;
                rhs(aa[0], aa[1]) += val * w * J;
            }
        }
    })
}

```

Listing 4: GPU IGA solver implementation

In its original C++ implementation *compute\_rhs()* function was implemented as it is presented in Listing 2.

The idea of this function consists of running the *for* loop on all  $E$  elements, and next in iterating through all  $Q$  quadrature points. At this place, there was the *for* iteration going through all local degrees of freedom  $A$  (corresponding to local matrix rows and columns) and calculating the appropriate values and putting them into the element array  $U$ . Next the values from the  $U$  arrays from various calls of the loop



`executor.for_each(elements(), [&](index_typee)` were added to the global result matrix.

The parallelization of this algorithm in its original implementation consists of parallel execution of calculations for individual elements  $E$ . At the end of every step, the synchronized execution of the summation ensured the correctness of data but, unfortunately, at the expense of extended computation time.

This type of code construction is not optimal for GPU execution. Frequent threads synchronization on the GPU card often results in even longer code execution than for the reference CPU code.

Therefore, following the GPU code execution patterns, the IGA algorithm has been slightly modified and is presented in Listing 3.

The proposed modification focuses on one of the most important disadvantages of the previous code, namely the aggregation of element matrices into the global matrix. In the previous version, in order to ensure the correct state of saved tables, synchronization was required when adding element matrices to the global matrix.

In the new version, no synchronization occurs at the time of saving the data. In this case, parallelization of calculations took place in the loop iterating over the global basis functions  $A$  (corresponding to global matrix rows), where each thread operates now on the loops iterating over all the elements in which the given global basis function  $A$  is defined. Finally, iteration over  $Q$  quadrature points occurs. This way, there is no need for any synchronization.

This solution is not without its drawbacks. Namely, this arrangement of *for* loop calls requires loading and recalculating certain pieces of data from memory many times. Nevertheless, the presented calculation scheme is very desirable from the point of view of GPU cards.

The final version dedicated to GPU cards was created as a combination of both the aforementioned approaches. A two-stage GPU algorithm was created and is presented in Listing 4. The first step uses the positive aspects of the solution presented in Listing 2. It allows us to calculate some values and then save them temporarily in GPU memory. The second step (reading these calculated values), allows us to perform the next time step calculation without synchronization.

```
void compute_rhs_post_V1() {
    int x = blockIdx.x *
        blockDim.x + threadIdx.x;
```

```

int y = blockIdx.y *
        blockDim.y + threadIdx.y;
int z = blockIdx.z *
        blockDim.z + threadIdx.z;
int3 quad_order = make_int3(
        getDimX_quad_order(),
        getDimY_quad_order(),
        getDimZ_quad_order());
int3 dofs = make_int3(
        getDimX_dofs(),
        getDimY_dofs(),
        getDimZ_dofs());
int3 elements = make_int3(
        getDimX_elements(),
        getDimY_elements(),
        getDimZ_elements());
...
float4 u = eval_fun(...);
...
}

```

Listing 5: Shared memory utilization: Less shared memory, more registers

```

void compute_rhs_post_V2() {
    __shared__ int3 quad_order, dofs, elements;
    __shared__ float4 u[256];
    int x = blockIdx.x *
        blockDim.x + threadIdx.x;
    int y = blockIdx.y *
        blockDim.y + threadIdx.y;
    int z = blockIdx.z *
        blockDim.z + threadIdx.z;
    if ((threadIdx.x==0)&&(threadIdx.y==0)&&(threadIdx.z
        ==0)) {
        quad_order = make_int3(
            getDimX_quad_order(),
            getDimY_quad_order(),
            getDimZ_quad_order());
        dofs = make_int3(

```

```

        getDimX_dofs() ,
        getDimY_dofs() ,
        getDimZ_dofs() );
elements = make_int3(
        getDimX_elements() ,
        getDimY_elements() ,
        getDimZ_elements() );
}
__syncthreads();
...
u[threadIdx.y * 16 + threadIdx.x] = eval_fun(...);
...
}

```

Listing 6: Shared memory utilization: More shared memory, less registers

Another critical element examined in the (original) solver is loading the same data many times repeatedly. In Listing 5, the first CUDA implementation of the algorithm discussed before is presented. In this implementation, it is assumed that each thread calculates the value for a particular row of the matrix. As it is shown, every time the calculation is performed every thread loads several three-dimensional variables responsible for configuring the calculation.

From the point of view of graphics cards, the problem is loading values for *quad\_core*, *dofs*, and *elements*. This action causes that these values are placed in registers allocated to individual threads at compilation time. As the GPU card has a specific architecture, it also has a set of many restrictions affecting the efficiency, such as limiting the maximum number of threads per block, the maximum number of threads per multiprocessor, the maximum number of 32-bit registers per multiprocessor, block and thread. And the last-mentioned limitation plays a key role in the implementation presented in Listing 5. The compiler during the compilation process is able to determine the required number of registers for each thread, and in case of too high demand, it limits the number of physically performed calculations at the same time on multiprocessors. This results in slowing down of the calculations.

The proposition of the more shared memory, fewer registers algorithm presented in Listing 6 is addressing this problem. The shared memory referred to in this algorithm is also a memory built on registers, but it is an additional memory block. One additional advantage of shared memory in

comparison to registers is the ability to access it through all threads in a given calculation block. Therefore, the proposition of the algorithm presented in Listing 6 is based on loading repeating constants into shared memory, so that the vast majority of registers are distributed to perform proper calculations so that the number of realistically parallel threads on a given multiprocessor is definitely greater than during the first implementation of the program.

The last detected IGA code retarder on graphics cards is the organization of the algorithm loops. Problematic from the GPU's point of view is the stop condition checking stage. When the *if* control statement is executed, all threads are synchronized and separated into two groups i.e. the ones who meet the condition and the others – what is important the second group has to wait until the first group finishes their job. In the consequence, there is a risk of synchronization of all threads working in a given block - what is the more so painful if there are nested loops or conditional statements in the code .

```
void compute_rhs_post_V1(int X, int Y){
    int x = blockIdx.x * blockDim.x + threadIdx.x;
    for(int y=0 ; y<Y ; ++y){
        for(int x=0 ; x<X ; ++x){
            M[y, x] = get_val(x,y);
        }
    }
    ...
}
```

Listing 7: Implementation with no unrolled loops

```
template<int X, int Y>
void compute_rhs_post_V2(){
    int x = blockIdx.x * blockDim.x + threadIdx.x;
    #pragma unroll
    for(int y=0 ; y<Y ; ++y){
        #pragma unroll
        for(int x=0 ; x<X ; ++x){
            M[y, x] = get_val(x,y);
        }
    }
    ...
}
```

Size	Time			Memory	
	CPU	GPU 1	GPU 2	CPU	GPU 2
$8^3$	0.06 s	0.01 s ( <b>x6</b> )	0.01 s ( <b>x6</b> )	88 MB	77 MB
$16^3$	0.52 s	0.03 s ( <b>x17.3</b> )	0.015 s ( <b>x34.6</b> )	89 MB	90 MB
$32^3$	4.18 s	0.09 s ( <b>x46.4x</b> )	0.04 s ( <b>x104.5</b> )	92 MB	141 MB
$64^3$	33.44 s	0.45 s ( <b>x74.3</b> )	0.22 s ( <b>x152</b> )	123 MB	354 MB
$128^3$	270 s	3.17 s ( <b>x85.2</b> )	1.6 s ( <b>x169</b> )	356 MB	1238 MB
$256^3$	2122 s	24.42 s ( <b>x86.9</b> )	12.39 s ( <b>x171.2</b> )	2185 MB	5050 MB

Table A.2: Time and memory consumption by IGA CPU and GPU solver versions.

```

void compute_rhs_post_V2_launch(int X){
    switch(X){
        case 1: compute_rhs_post_V2<1, 1>(); break;
        case 2: compute_rhs_post_V2<2, 2>(); break;
    }
}

```

Listing 8: Implementation with unrolled loops

In the case of the IGA algorithm presented in Listing 7, it can be seen that the standard implementation of this algorithm (in particular for three-dimensional space) can generate a fairly deeply nested *for* instructions. Fortunately, in its specification, the CUDA programming language has a directive requiring the compiler to unroll a loop. Unrolling the loop means, in fact, pasting subsequent iterations of the *for* loop body as many times as the condition of the loop indicates so that the final code does not have the repetitive conditional *if* instructions. To be able to achieve this type of unrolling, at the compilation time, the final value with which the current state of the loop counter is compared is required. Unfortunately, in the presented solution providing such a specific value is impossible because it is obtained from the dynamically loaded configuration. The algorithm schema presented in Listing 7 solves this problem. In practice, during compilation, functions are expanded for all possible configurations of the parameter passed using template parameters. As a result, it is possible to reduce the number of nested loops and significantly speed up the program.

In Table A.2 speed-up and memory consumption for CPU original implementation presented in Listing 2 and for GPU optimized version from Listing 8, are presented for one and two GPUs. The GLUON library [15]

glues several instances of GPU tumor simulators, executed on different GPUs, so they can simulate larger problems. Experiments have been performed on Prometheus supercomputer [16, 17], where CPU means Intel Xeon E5-2680v3 processor and GPU means Nvidia Tesla K40 XL. As one may see for  $256^3$  dimension, the speed-up of more than 171 times can be observed.

## References

- [1] E. A. B. F. Lima, J. T. Oden, B. Wohlmuth, A. Shamoradi, D. A. Hormuth II, T. E. Yankeelov, L. Scarabosio, T. Horger, *Selection and Validation of Predictive Models of Radiation Effects on Tumor Growth Based on Noninvasive Imaging Data*, Computer Methods in Applied Mechanics and Engineering, 327 (2017) 277-305.
- [2] M. Welter, H. Rieger, *Physical determinants of vascular network remodeling during tumor growth*, The European Physical Journal E, 33(2), 149-163 (2010)
- [3] M. A. Chaplain, S. R. McDougall, A. R. A. Anderson, *Mathematical modeling of tumor induced angiogenesis*, Annual Review of Biomedical Engineering 8 (2006) 233-257.
- [4] A. R. A. Anderson, M. A. J. Chaplain, *Continuous and discrete mathematical models of tumor-induced angiogenesis*, Bulletin of Mathematical Biology, 5(60) (1998) 857-899.
- [5] M. A. Rupnick, C. L. Stokes, S. K. Williams, D. A. Lauffenburger, *Quantitative analysis of human microvessel endothelial cells using a linear under-agarose assay*, Laboratory Investigation; a Journal of Technical Methods and Pathology, 59 (1998) 363-372.
- [6] R. Wcisło, W. Dzwinel, D. A. Yuen, A. Z. Dudek, *3-D model of tumor progression based on complex automata driven by particle dynamics*, Journal of Molecular Modeling, 15(12) (2009) 1517-1539.
- [7] V. Andasari, A. Gerisch, G. Lolas, A. P. South, M. A. Chaplain, *Mathematical modeling of cancer cell invasion of tissue: biological insight from mathematical analysis and computational simulation*, Journal of Mathematical Biology, 63(1) (2011) 141-171

- [8] M. Łoś, M. Paszyński, A. Kłusek, W. Dzwinel, *Application of fast isogeometric  $L_2$  projection solver for tumor growth simulations*, Computer Methods in Applied Mechanics and Engineering 316 (2017) 1257-1269
- [9] V. Puzyreva, M. Łoś, G. Gurgul, V. M. Calo, W. Dzwinel, M. Paszyński, *Parallel splitting solvers for the isogeometric analysis of the Cahn-Hilliard equation*, Computer Methods in Biomechanics and Biomedical Engineering (2019) submitted.
- [10] X. Wu, G. J. van Zwieten, K. van der Zee K, *Stabilized second-order convex splitting schemes for Cahn-Hilliard models with application to diffuse-interface tumor-growth models*, Numerical Methods in Biomechanical Engineering, 30(3) (2014) 180-203.
- [11] K. G. van der Zee, J. T. Oden, S. Prudhomme, A. Hawkins-Daarud, *Goal-oriented error estimation for Cahn-Hilliard models of binary phase transition*, Numerical Methods for Partial Differential Equations. 27(1) (2011) 160-196.
- [12] M. Łoś, A. Kłusek, M. A. Hassaan, K. Pingali, W. Dzwinel, M. Paszyński, *Parallel fast isogeometric  $L_2$  projection solver with GALOIS system for 3D tumor growth simulations*, Computer Methods in Applied Mechanics and Engineering, 343, (2019) 1-22
- [13] F. M. Selten, F. J. Schevenhoven, G. S. Duane, *Simulating climate with a syn-chronization-based supermodel*, Chaos 27, 126903 (2017)
- [14] A. Kłusek, M. Łoś, M. Paszyński, W. Dzwinel, *Efficient model of tumor dynamics simulated in multi-GPU environment*, The International Journal of High Performance Computing Applications, 33(3) (2019) 1-18.
- [15] R. Dathathri, G. Gill, L. Hoang, H.-V. Dang, A. Brooks, N. Dryden, M. Snir, K. Pingali, *GLUON: A Communication - Optimizing Substrate for Distributed Heterogeneous Graph Analytics*, Proceedings of the 39th ACM SIGPLAN Conference on Programming Language Design and Implementation (PLDI) (2018)
- [16] <http://www.cyfronet.krakow.pl/computers/15226,artykul,prometheus.html> (accessed on June 2019)

- [17] M. Bubak, J. Kitowski, K. Wiatr, *E-Science on Distributed Computing Infrastructure*, Achievements of PL-Grid Plus Domain-specific Services and Tools, Volume 8500 (2014) Springer
- [18] Galois Framework. <http://iss.ices.utexas.edu/?p=projects/galois>
- [19] K. Pingali, D. Nguyen, M. Kulkarni, M. Burtscher, M.A. Hassaan, R. Kaleem, T.H. Lee, A. Lenharth, R. Manevich, M. Mendez-Lojo, D. Pountzos, X. Sui, The tao of parallelism in algorithms, in Proceedings of the 32nd ACM SIGPLAN Conference on Programming Language Design and Implementation (2011) 12-25
- [20] W. Dzwinel, A. Kłusek and M. Paszyński, *A concept of a prognostic system for personalized anti-tumor therapy based on supermodeling*, Procedia Computer Science, 108C (2017) 1832–1841
- [21] W. Dzwinel, A. Kłusek, O. V. Vasilyev, *Supermodeling in simulation of melanoma progression*, Procedia Computer Science, 80 (2016) 999-1010.
- [22] A. Kłusek, M. Łoś, M. Paszyński, W. Dzwinel, *Efficient model of tumor progression simulated in multi-GPU environment*, International Journal of High Performance Computing Applications, 33(3) (2019) 489-506.
- [23] E. Kalnay, *Atmospheric modeling, data assimilation and predictability*, Cambridge university press. (2003)
- [24] G. Evensen, *Data assimilation: the ensemble Kalman filter*. Springer Science & Business Media (2009)
- [25] K. Law, A. Stuart, K. Zygalakis, *Data assimilation*, Cham, Switzerland, Springer. Reich (2015)
- [26] S. Reich, C. Cotter, *Probabilistic forecasting and Bayesian data assimilation*, Cambridge University Press (2015)
- [27] W. Wiegerinck, F. Selten, *Supermodeling: Combining imperfect models through learning*, NIPS Workshop on Machine Learning for Sustainability (MLSUST) (2011)



- [28] M. L. Shen, N. Keenlyside, F. Selten, W. Wiegnerinck, G. S. Duane, *Dynamically combining climate models to "supermodel" the tropical Pacific*, Geophysical Research Letters, 43(1) (2016) 359-366
- [29] B. P. Kirtman, N. L. Perlin, L. Siqueira, *Ocean eddies and climate predictability*, Chaos: An Interdisciplinary Journal of Nonlinear Science, 27, 126902 (2017)
- [30] M. L. Shen, N. Keenlyside, B. C. Bhatt, G. S. Duane, *Role of atmosphere-ocean interactions in supermodeling the tropical Pacific climate*, Chaos: An Interdisciplinary Journal of Nonlinear Science, 27, 126704 (2017)
- [31] A. Saltelli, S. Tarantola, F. Campolongo, M. Ratto, *Sensitivity analysis in practice: a guide to assessing scientific models* Chichester, England (2004)
- [32] L. Siwik, M. Łoś, A. Klusek, W. Dzwiniel, M. Paszyński, *Tuning two-dimensional tumor growth simulations*, 2018 Summer Simulation Multi-conference, Bordeaux, France, July 9–12, (2018)
- [33] L. Kocarev, *Consensus and synchronization in complex networks*, Springer (2013)
- [34] B. Ribba, E. Watkin, M. Tod, P. Girard, E. Grenier, B. You, E. Giraudo, G. Freyer, A model of vascular tumour growth in mice combining longitudinal tumour size data with histological biomarkers, European Journal of Cancer, 47(3) (2011) 479-490.
- [35] W. Dzwiniel, A. Klusek, O.V. Vasilyev, Supermodeling in Simulation of Melanoma Progression, Procedia Computer Science, 80, 2016, pp.999-1010
- [36] T. Bäck, Evolutionary Algorithms in Theory and Practice: Evolution Strategies, Evolutionary Programming, Genetic Algorithms, Oxford University Press, Inc., 1996
- [37] M. Smolka, E. Gajda-Zagorska, R. Schafer, M. Paszynski, D. Pardo, A hybrid method for inversion of 3D AC resistivity logging measurements, Applied Soft Computing, 36(2015) 442–456.

- [38] M.D. Vose, The Simple Genetic Algorithm: Foundations and Theory, MIT Press, 1998